Pretest Computational Assessment of Boundary Layer Transition in the NASA Juncture Flow Model with an NACA 0015-Based Wing

Balaji Shankar Venkatachari,[*] Pedro Paredes[†]
National Institute of Aerospace, Hampton, VA 23666

Meelan Choudhari,[‡] Fei Li,[§] and Chau-Lyan Chang[**]
NASA Langley Research Center, Hampton, VA 23681

The first two phases of the NASA Juncture Flow experiment were carried out on a DLR-F6 swept-wing model and were designed to provide "CFD validation-quality" data toward the assessment and improvement of existing CFD turbulence models in predicting onset and extent of three-dimensional separated flow near the wing-juncture trailing-edge region. The next phase of experiments will involve an NACA 0015-based swept wing, as prior risk reduction experiments had indicated that this wing shape resulted in reduced separation near the juncture region than the DLR-F6 wing, thus providing a better option to evaluate the ability of CFD models to predict incipient turbulent separation. The NACA 0015 measurements will also include IR thermography to infer the variation of transition front with respect to an increasing angle of attack. The primary objective of this work is to computationally make a preliminary assessment of the transition front on both surfaces of the NACA 0015 wing at a crank-chord-based Reynolds number of 2.4 x 10^6 for four different angles of attack, (0°, 2.5°, 5°, and 7.5°) and to determine the dominant mechanisms responsible for transition. This assessment includes both RANS-based transition models from NASA's OVERFLOW 2.3b flow solver and linear parabolized stability equations (PSE) stability analysis based on the Langley Stability and Transition Analysis code, LASTRAC. Linear PSE results indicate that the upper surface of the wing is dominated by Tollmien-Schlichting (TS) instabilities, and that the laminar flow region shrinks from about 50% chord to a very small region just downstream of the attachment line as the angle of attack is increased from 0° to 7.5°. Consequently, the transition fronts predicted by the Spalart-Allmaras-based amplification factor transport (AFT-2017b) equation model (which accounts for the TS instabilities alone) and the Menter's shear-stress transport equation (SST2003)-based Langtry-Menter transition model with ability to account for both TS and crossflow effects (LM2015) compare well with those predicted using linear PSE. On the lower surface of the wing, stationary crossflow (CF) instabilities begin to appear on the inboard portion of the wing in addition to the TS-instabilities for the larger angles of attack (5° and 7.5°), further reducing the laminar flow extent within the inboard region. The LM2015 model that accounts for CF effects is able to replicate this trend but appears to predict a slightly earlier transition. The outcome of this effort will inform the experiment and, when the actual experimental data become available, provide further opportunity to assess and improve the various transition models.

---

[*] Sr. Research Engineer, Email: balaji.s.venkatachari@nasa.gov, Senior member, AIAA

[†] Sr. Research Engineer, Email: pedro.paredesgonzalez@nasa.gov, Member, AIAA

[‡] Aerospace Technologist, Computational AeroSciences Branch, Email: m.m.choudhari@nasa.gov, Fellow, AIAA

[§] Aerospace Technologist, Computational AeroSciences Branch, Email: Fei.Li@nasa.gov

[**] Aerospace Technologist, Computational AeroSciences Branch, Email: chau-lyan.chang@nasa.gov, Associate Fellow, AIAA

Nomenclature

C_D	=	drag coefficient [nondimensional]
C_f	=	skin-friction coefficient [nondimensional]
C_L	=	lift coefficient [nondimensional]
C_m	=	pitching moment coefficient [nondimensional]
C_p	=	surface pressure coefficient [nondimensional]
M	=	Mach number [nondimensional]
N	=	logarithmic amplification factor
$\overline{q}$	=	vector of base flow variables
$\tilde{q}$	=	vector of perturbation variables
$\hat{q}$	=	vector of amplitude variables
T	=	Temperature [K]
(u,v,w)	=	streamwise, wall-normal, and spanwise velocity components [m s^{-1}]
(x, y, z)	=	Cartesian coordinates [m]
x/c	=	chordwise coordinate scaled by reference chord length [nondimensional]
y^{+}	=	near wall grid spacing in wall units [nondimensional]
α	=	angle of attack [deg], streamwise wavenumber [m^{-1}]
β	=	spanwise wavenumber [m^{-1}]
λ	=	spanwise wavelength [m]
μ	=	dynamic viscosity [kg/(m.s)]
μ_t	=	turbulent eddy viscosity [kg/(m.s)]
ω	=	disturbance angular frequency [rad s^{-1}]
ρ	=	density [kg m^{-3}]
σ	=	spatial growth rate [m^{-1}]
(ξ, η, ζ)	=	streamwise, wall-normal, and spanwise coordinates [m]
Subscript		
0	=	neutral/critical point
c	=	critical value
Superscript		
H	=	conjugate transpose

I. Introduction

According to the CFD Vision 2030 [1], the most critical area in computational fluid dynamics (CFD) simulation capability that will remain a pacing item for the foreseeable future is the ability to adequately predict viscous flows with boundary layer transition and flow separation. A majority of CFD computations are carried out under the assumption that the flow is turbulent everywhere, and they often use the computationally efficient Reynolds-averaged Navier-Stokes (RANS) models. However, for certain applications such as wings with natural laminar flow (NLF) technology or unmanned aerial vehicle design, such strong assumptions can lead to significant errors in performance estimation. Furthermore, most of the RANS models are incapable of modeling the process of laminar-to-turbulent boundary layer transition because of the complexity involved in the physics of the transition onset process, and the inherent averaging process in the RANS procedure makes it difficult to capture the development of the linear disturbances and its subsequent nonlinear growth and eventual breakdown. Even in the case of fully turbulent flow, the RANS models are incapable of accurately predicting the onset and extent of fully-separated flows that often arise near the trailing-edge of an airplane wing near the wing-root junction or the wing-pylon intersection. With these aspects in mind, NASA has recently embarked on conducting a series of experiments [2–10] aimed at providing CFD validation quality flow-field data (including detailed characterization of boundary conditions, quantification of experimental uncertainties etc.) to help assess and improve existing turbulence models.

The NASA juncture Flow experiment [2–6] is one such series of wind tunnel tests, conducted in the NASA Langley 14- by 22-Foot Subsonic Tunnel between late 2017 and Spring 2020, designed to provide detailed flow-field data along with quantified boundary conditions, geometry, and measurement uncertainties regarding the separated flow that occurs near the wing-juncture trailing-edge region. The primary objective

of the experiment was aimed at validating, assessing, and improving CFD turbulence models with regards to prediction of such separated flows. The first two phases of this experimental campaign have been completed and were on a generic full-span wing-fuselage junction model at subsonic conditions, with the wing being modeled after the DLR-F6. Furthermore, in these experiments, the boundary layer was tripped near the front of the fuselage and on both surfaces of the wing. As part of AIAA Scitech and Aviation 2020, special sessions focusing on CFD results obtained with RANS and scale-resolving methods and its comparison against measured experimental data were also organized. All the associated publications have been documented in the NASA Juncture Flow website.[††] The next phase of the NASA juncture flow experiment is expected to be carried out in early 2022, with a wing based on the NACA 0015 airfoil at the root. The NACA 0015-based wing is expected to yield a much smaller separation than the F6-based wing, thereby providing data for evaluation of the CFD model's ability to capture incipient separation [3]. Additionally, as part of the experimental campaign, there are plans to measure the transition location on the untripped swept wing over a range of angles of attack, using IR thermography. As a result, this new series of experiments is expected to help the assessment of RANS turbulence models as well as RANS-based transition prediction models.

RANS-based transition prediction models [11–21] have gained in popularity over alternate approaches such as direct numerical simulations (DNS), wall-resolved large-eddy simulations (WRLES), stability-theory-based approaches like the e^N method [22–25] or parabolized stability equations (PSE) [26]. Primary reasons for this wide adoption of RANS-based approaches are: (i) less stringent grid resolution requirements within the boundary layer; (ii) reduced computational cost; (iii) use of localized information, allowing for massive parallelization and the use of unstructured grids; and (iv) less reliance on user expertise (as opposed to that needed for stability-theory-based approaches, such as an adequate understanding of the transition physics and hydrodynamic stability theory). The RANS-based transition models often rely on solving additional transport equations and using correlations that determine the onset of transition, allowing the codes to switch between operating in the laminar and turbulent modes. This approach clearly overcomes some of the aforementioned limitations of stability-based transition prediction and is well-suited for generalizing the established process for turbulent flow computations in a cost-effective manner. However, by virtue of lacking an adequate representation of the complex transition process, such models often rely upon correlations derived from a limited number of low-speed experiments or data derived from stability theory and do not account for all the transition mechanisms and/or their variation with the significant flow parameters, thereby being less amenable to an extrapolation to new configurations and must be validated on a case by case basis in general. Thus, any additional quality data from experiments performed with CFD validation as the primary objective would help evaluate and improve the accuracy of these transport-equation-based transition models. Further details on the various approaches currently being used to predict/model transition can be found in Refs. [27,28].

The primary purpose of the current work is to perform pretest CFD computations at selected flow conditions for the NACA 0015-based NASA Juncture flow model by using the RANS-based transition modeling capability available within NASA's OVERFLOW 2.3b code [29] and to augment those computations via detailed stability analysis of the boundary layer flow over the wing by using NASA's LASTRAC stability software [30, 31]. This effort should reveal important flow features, indicate the dominant transition mechanisms, and characterize the influence of transition on the onset and the size of the separated flow, hence informing the wind tunnel test. More importantly, such an effort will help with a blind assessment of the transition prediction tools before the actual experimental data becomes available. Such an assessment will help identify the gaps in the current models and, hence, contribute to our ongoing assessment and refinement of the various transition models for swept wing configurations [32, 33, 34].

The paper is organized as follows. Sections II-IV provide details about the model configuration, the flow solver, stability analysis tools, the transition models, and the flow conditions investigated. That is followed by a discussion of the results from the stability analysis and RANS-based transition model in Section V. The conclusions are provided in section VI.

II. NASA Juncture Flow Model with the NACA 0015-based Wing

The model is a full-span wing-fuselage body and has the same fuselage as that used in the first two phases of the experimental campaign with a nominal length of 4839±2 mm. The wing shape is based on the NACA 0015 airfoil with a wing span (tip-to-tip) of 3327±2 mm, has no dihedral and also includes an inboard,

---

[††] https://turbmodels.larc.nasa.gov/Other_exp_Data/junctureflow_exp.html

leading-edge horn. The crank chord was 581±1 mm and the leading-edge wing sweep was approximately 37.3 degrees. The entire configuration was top-bottom symmetric, unlike the F6-based wing. All of the tests are expected to be carried out at the NASA Langley 14- by 22-Foot Subsonic Tunnel, which is a closed-circuit atmospheric-pressure wind tunnel, with the crank chord-based Reynolds number expected to be fixed at 2.4 Million throughout the tests. More details on the model geometry and about the experiments can be found on the NASA Juncture Flow website.[‡‡]

III. Flow Solver, Transition Models and Stability Analysis Tools

NASA's OVERFLOW 2.3b [29], an implicit structured overset grid Navier-Stokes solver that is capable of computing time-accurate and steady-state solutions via a variety of options for spatial and temporal discretization, is used to obtain the mean flow for performing the stability analysis as well as for computations involving RANS-based transition models.

A. Stability Analysis

Stability analysis of the boundary layers over the wing is studied with the nonorthogonal curvilinear coordinate system as implemented in the LASTRAC.3D code [30]. The nonorthogonal curvilinear coordinate system allows the selection of surface coordinates to be roughly aligned with the streamwise direction and along the spanwise surface grid lines (which run parallel to the leading and trailing edges) in the spanwise direction. The remaining coordinate is defined in the wall normal direction. Results for boundary layers over infinite-swept-wing configurations have been shown to be identical between the orthogonal and nonorthogonal coordinate systems [30]. In conventional quasiparallel linear stability theory (LST), the boundary layer is assumed to be locally parallel by dropping the streamwise derivative terms and setting the wall-normal velocity derivative equal to zero. However, here we use the PSE approach, where the streamwise and spanwise curvature, along with nonparallel effects are also considered.

The PSE approximation is based on isolating the rapid phase variations in the streamwise directions. The effects of instability wave propagation within a fully three-dimensional boundary layer can also be evaluated by performing the parabolic integration along stream or group velocity lines. The variables (ξ, η, ζ) denote the streamwise, wall-normal, and spanwise directions in the nonorthogonal coordinates and (u, v, w) representing the corresponding velocity components. Density and temperature are denoted by ρ and T. The Cartesian coordinates are represented by (x, y, z), respectively. The vector of perturbation fluid variables is $\widetilde{\boldsymbol{q}}(\xi, \eta, \zeta, t) = \left(\tilde{\rho}, \tilde{u}, \tilde{v}, \tilde{w}, \widetilde{T}\right)^T$, and the vector of amplitude functions is $\widehat{\boldsymbol{q}}(\xi, \eta, \zeta) = \left(\hat{\rho}, \hat{u}, \hat{v}, \hat{w}, \hat{T}\right)^T$, and the vector of basic state fluid variables is $\bar{\boldsymbol{q}}(\xi, \eta, \zeta) = \left(\bar{\rho}, \bar{u}, \bar{v}, \bar{w}, \bar{T}\right)^T$. The streamwise and spanwise wave numbers are α and β, respectively, and ω is the angular frequency of the perturbation. The spanwise wavelength is defined as $\lambda = 2\pi/\beta$. The perturbations have the form

$$\widetilde{\boldsymbol{q}}(\xi, \eta, \zeta, t) = \widehat{\boldsymbol{q}}(\xi, \eta) exp\left[i\left(\int_{\xi_0}^{\xi} \alpha(\xi')d\xi' + \beta\zeta - \omega t\right)\right], \qquad (1)$$

where the unknown, streamwise varying wavenumber $\alpha(\xi)$ is determined in the course of the solution by imposing a normalization condition, that implies a slow variation of the amplitude functions $\widehat{\boldsymbol{q}}(\xi, \eta, \zeta)$ in the streamwise direction in comparison with the phase term $exp\left[i\int_{\xi_0}^{\xi} \alpha(\xi')d\xi'\right]$. Substituting Eq. (1) into the linearized Navier-Stokes equations and involving the scale separation to neglect the viscous, streamwise derivative terms, one obtains the PSE in the form

$$\left(\mathbf{L} + \mathbf{M}\frac{\partial}{\partial\xi}\right)\widehat{\boldsymbol{q}}(\xi, \eta) = 0 \qquad (2)$$

The entries of the coefficient matrices for $\mathbf{L}$ and $\mathbf{M}$ with a more detailed description of the method can be found in the Refs. [27, 30, 31]. In this work, the local line-marching approach, where the PSE marching is performed along a preidentified streamline path along the surface, has been adopted. More details on this approach can be found in Ref. [30]. The nonparallel growth rate of the disturbances along a streamline with a selected combination of ω and β is defined as

---

[‡‡] https://turbmodels.larc.nasa.gov/Other_exp_Data/JunctureFlow_0015/junctureflow_0015_exp.html

$$\sigma_{\text{PSE}}(\xi, \omega, \beta) = -\Im(\alpha) + \frac{1}{2}\frac{dK}{d\xi}, \tag{3}$$

where K is based on the Kinetic energy norm.

1. The Dual N-factor Method

The onset of laminar-turbulent transition is estimated using the logarithmic amplification ratio, the so-called N-factor, relative to the lower bound location ξ_{lb} where the disturbance first becomes unstable,

$$N(\omega, \beta) = -\int_{\xi_{lb}}^{\xi} \sigma(\xi', \omega, \beta)d\xi'. \tag{4}$$

Here, we assume that transition onset is likely to occur when a function of N-factor envelope values based on stationary crossflow instability waves, N_{CF}, and based on travelling Tollmien-Schlichting instability waves, N_{TS}, reaches a certain threshold [34–36]. The expression of the dual $N_{CF} - N_{CF}$ criterion can be written as

$$\left(\frac{N_{TS}}{N_{TS,c}}\right)^{a_{TS}} + \left(\frac{N_{CF}}{N_{CF,c}}\right)^{a_{CF}} = 1, \tag{5}$$

where the subscript c refers to the critical value, and the exponents a_{TS} and a_{CF} control the level of interaction between the two types of instability waves.

B. RANS-based Transition Models

RANS-based transition models available in OVERFLOW 2.3b include: (i) the two-equation Langtry-Menter transition model (LM2009) [14,15] based on the year 2003 version of Menter's shear-stress transport (SST) RANS model [36,37], along with the modifications proposed by Langtry et al. [39] to account for crossflow induced transition (LM2015); (ii) Coder's [19, 20] 2017b version of the amplification factor transport (AFT 2017b) equation-based model that uses the Spalart-Allmaras (SA) model [40]; and (iii) the Medida-Baeder model [16], which is a reformulation of the Langtry-Menter transition model to allow its integration with the SA model. The AFT and Medida-Baeder models, as implemented in OVERFLOW, can only account for Tollmien-Schlichting (TS) waves induced transition and cannot account for crossflow effects. As alternate implementations of crossflow models [41–46] to explore crossflow effects induced by mechanisms other than roughness are not available under OVERFLOW 2.3b, the LM model (LM2015 mainly) and the AFT2017b model are primarily used as part of this research work. According to the nomenclature of NASA's turbulence modeling resource,[§§] these transition models should ideally be referred to as SA-AFT2017b and SST-2003-LM2009/LM2015, respectively. However, for sake of brevity, they will be referred to as AFT2017b and LM2009/LM2015 throughout this work.

IV. Flow Conditions and Grid Details

The flow conditions investigated as part of this work. correspond to a freestream temperature of 288.84K, Mach number of 0.189, a Reynolds number based on the crank chord (MAC) equal to 2.4 x 10^6, and four different angles of attack: 0°, 2.5°, 5°, and 7.5°, respectively. These conditions match some of the planned test conditions for the experiment. The free stream turbulence intensity (FSTI) was prescribed to be 0.08% based on previous characterization of the tunnel [47], and the surface roughness of the model was specified to be 3.3 μm based on the roughness levels generally seen on a painted surface [48].

While the original model is full span, the computation carried out on a semispan geometry under the assumption of symmetry being enforced on the x-z plane. The baseline mesh for the semispan geometry used in these computations had seven overset near-body blocks (three on the fuselage, including its nose and tail, one wing-body collar grid, and three on the wing, including its tip), as shown in Fig. 1. The generation of off-body grids and hole cutting were carried out by using OVERFLOW's domain connectivity function (DCF) approach. The wing and fuselage near-body grids had 325 points in the wall-normal direction with a

---

[§§] https://turbmodels.larc.nasa.gov

near-wall spacing of 2.6 x 10^{-3} mm ($y+ = 0.5$), a growth rate of 1.02, and the initial 10 grid points near the wall being uniformly spaced. It also contained 433 points around the wing in the chordwise direction (25 points in the trailing edge) and 463 points in the spanwise direction. The near-body grid had an overall grid count of approximately 140 million points. The far-field boundaries of the outer-body grids were placed at approximately 100 crank chords. In addition to the baseline grid, a coarser and finer grid were also generated through uniform refinement toward a grid convergence study. The coarser grid contained two-thirds the number of points in each of the three directions as that of the baseline grid, while the finer grid had 1.5 times the number of points in each of the three directions as that of the baseline grid, respectively. Adiabatic wall, symmetry, and freestream boundary conditions were used for the computations.

V. Results

We begin by presenting the mean flow solutions that are needed for the stability analysis of the boundary layer at the selected flow conditions. Then, the instability characteristics of those mean flows are analyzed by using the PSE formulation and the transition front is determined using the *N*-factor values determined from the analysis. Subsequently, results from computations using the RANS-based transition models are presented and compared against results from the stability analysis. All the solutions were obtained by running the OVERFLOW solver in a steady-state manner by using the 3rd-order Roe upwind scheme [49] and the unfactored successive symmetric overrelaxation (SSOR) implicit solution algorithm [50].

In the following sections, surface pressure (and skin friction) variations at various spanwise locations indicated in Fig. 2 are often used to get an understanding of the flow at the selected flow conditions, and to compare the results obtained using the different approaches.
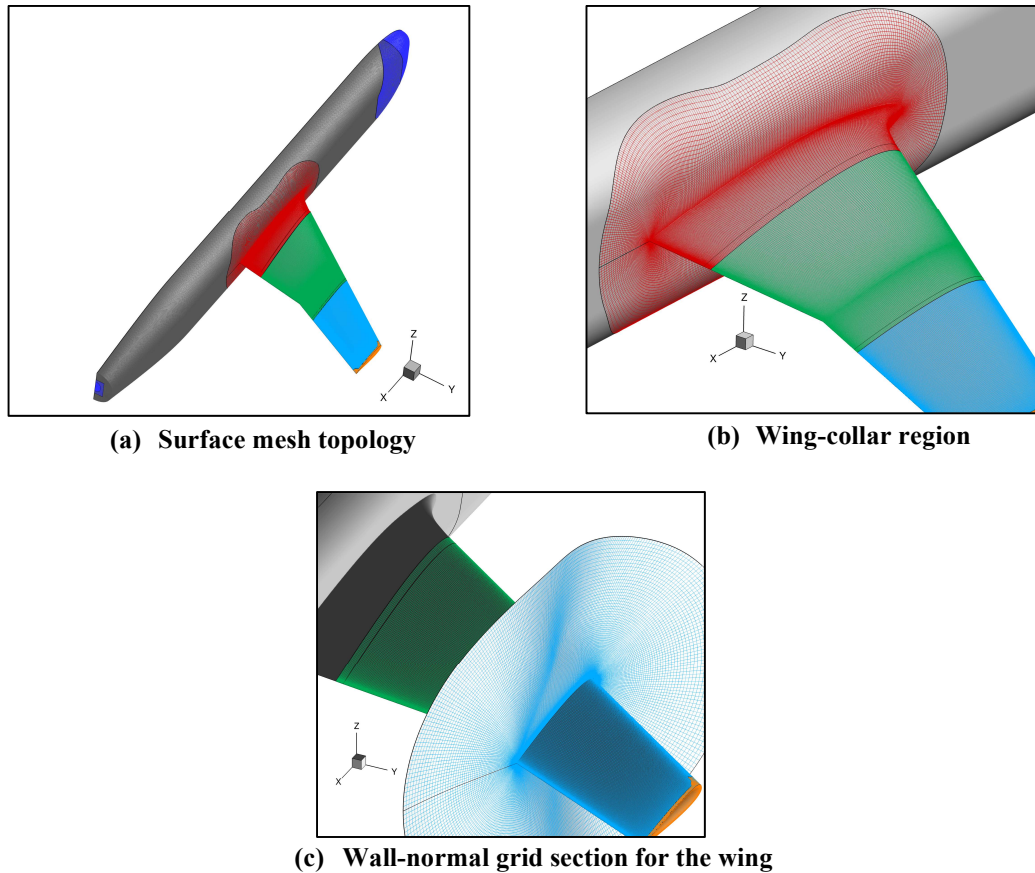

(a) Surface mesh topology

(b) Wing-collar region

(c) Wall-normal grid section for the wing

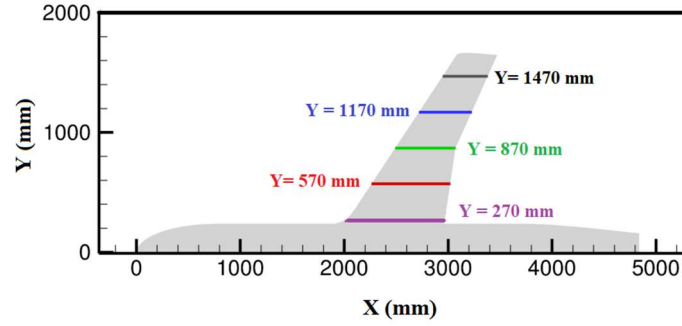Fig. 1. Overview of the near-body mesh.

6

**Fig. 2. Spanwise stations where surface pressure data are compared.**

A. Mean Flow Solutions

The mean flow computations at the desired flow conditions were carried out by using the Spalart-Almaras RANS model with Rotation-Curvature correction (RC) [51], quadratic constitutive relation (QCR2000) [52], along with imposition of the transition front on the wings. Under these settings, the boundary layer remains laminar until the specified location of the transition. The transition front was specified such that one obtained maximum laminar flow extent, without any flow separation. This can be achieved by either running the flow under laminar assumption and setting the transition location upstream of where separation occurred or using the pressure distribution obtained from a fully turbulent simulation, to set the transition front as far downstream as possible from the suction peak to not cause any separation. This process may require multiple iterations. The fuselage itself was run fully turbulent (letting the model automatically transition from laminar-to-turbulent without specifying any trip locations).

Figure 3 shows the contours of the pressure coefficient over the semispan juncture flow model with the NACA0015-based wing for the computation with an imposed transition front at different angle of attack conditions. To gain a better understanding of the pressure distribution across the wing, the distribution at selected spanwise locations on the wing are also shown in Fig. 4. From Figures 3 and 4, it can be inferred that if one ignores the region close to the root of the wing (see the results at $y = 270$mm in Fig. 4), the flow over the upper surface of the wing undergoes quick acceleration near the leading edge at all angles of attack, with the downstream portion of the wing being under an adverse pressure gradient that becomes stronger with an increasing angle of attack. Near the root of the wing, the suction peak appears to be further downstream from the leading edge and only at $\alpha = 7.5°$ does the suction peak appear to be at the leading edge. Furthermore, at $\alpha = 7.5°$, near the root of the wing, there appears to be a small region of weak adverse pressure gradient followed by a weak favorable pressure gradient region, before switching to an adverse pressure gradient region completely along the chordwise direction. On the lower surface of the wing, all the spanwise locations appear to experience a region of acceleration followed by a region of weak adverse pressure gradient. For $\alpha = 7.5°$, between $x/c = 0.2$ and 0.8, the pressure appears to be nearly constant. For $\alpha = 0°$, with the NACA 0015-based wing being symmetric in geometry, the pressure distribution on both the upper and the lower surface are identical. The forces and the pitching moment coefficients for the computations with an imposed transition are listed in Table 1 for the different flow conditions.

To ensure that the solutions of the mean flow utilized for the stability analysis are grid converged, the computations were repeated using the coarse, baseline and fine grids for $\alpha = 5°$ by imposing the transition front on the wing at identical locations (to the extent permitted by the grid resolution). The distribution of pressure and skin-friction coefficient along the streamwise direction at selected spanwise stations are shown in Fig. 5 and they all collapse well with each other. The transition location on the upper surface for coarse grid alone appears to be slightly downstream by a distance of less than 3% local chord. The net effect from this is that the mean flow used in the stability analysis will have a slightly larger laminar region, but that will not affect the overall prediction themselves. The reasonable agreement between the solutions obtained with various grid resolutions indicates that the baseline grid has adequate resolution for use with stability analysis. The force and moment coefficients obtained with these different grids are listed under Table 2 and indicate that the lift and drag coefficients also compare reasonably well with each other. However, the pitching moment coefficient obtained with the fine grid is much higher than the value obtained with either the baseline or coarse grid and it was not clear as to what was causing it. Looking into the loading on the wing component of the model alone, it appeared that there was reasonable match between the forces and moment coefficients

7

obtained using the three different grids. Thus, the shift in pitching moment must be coming from the fuselage component and needs further investigation.

(a) $\alpha = 0°$

(b) $\alpha = 2.5°$

**(c)** $\alpha = 5°$

(d) $\alpha = 7.5°$
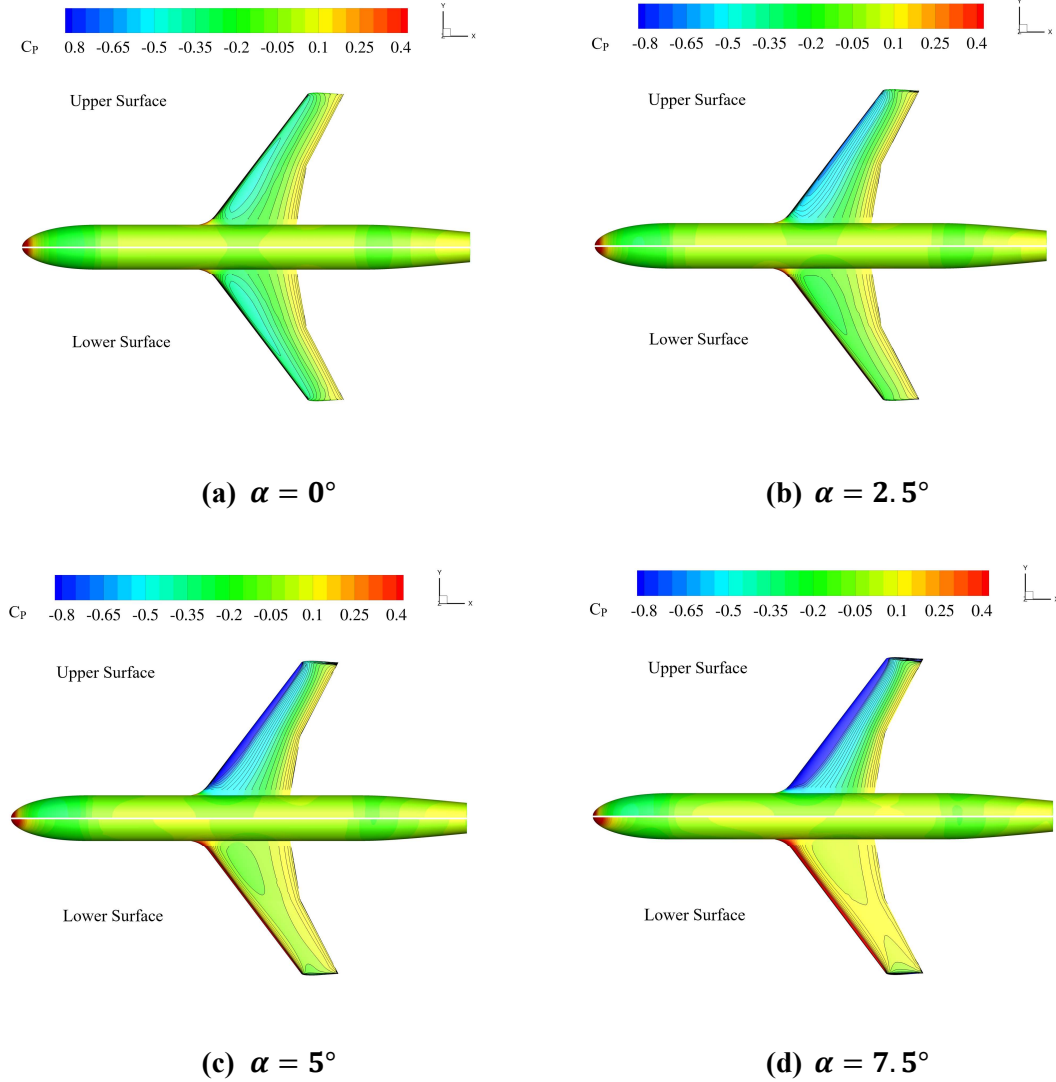
Fig. 3. Surface pressure distribution contours for the selected flow conditions on the baseline grid. The contour lines are also shown on the wing portion.

Table 1 Force and moment coefficients for the baseline grid computations with an imposed front.

Angle of Attack	C_L	C_D	C_m
$\alpha = 0.0°$	-0.00213	0.02183	0.00108
$\alpha = 2.5°$	0.19456	0.02486	-0.01519
$\alpha = 5.0°$	0.39460	0.03321	-0.03798
$\alpha = 7.5°$	0.57909	0.04490	-0.05494
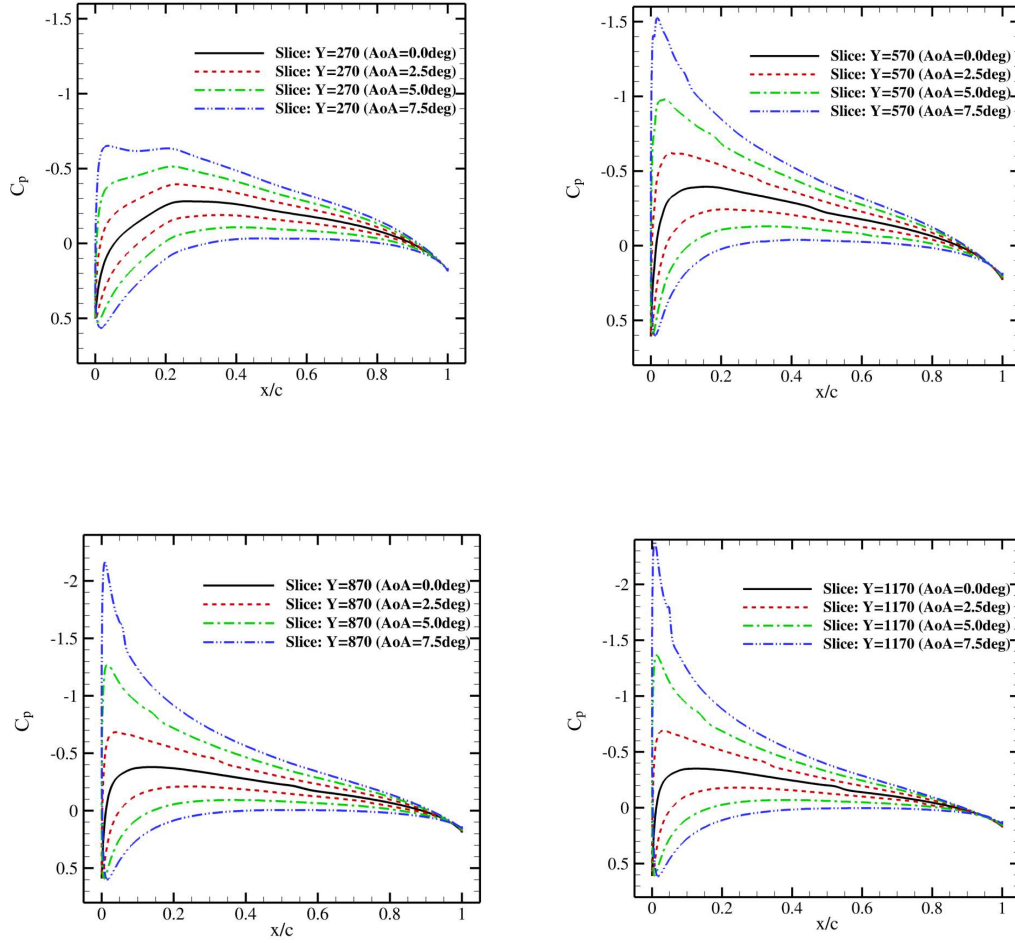
Fig. 4. Variation of surface pressure distribution on the baseline grid with change in angle of attack at selected spanwise stations on the wing.

Table 2 Force and moment coefficients for the computations with an imposed front using different grid resolution for $\alpha = 5°$.

	C_L	C_D	C_m
Coarse Grid	0.38659	0.03274	-0.03776
Baseline Grid	0.39460	0.03321	-0.03798
Fine Grid	0.41375	0.03340	-0.05234

9
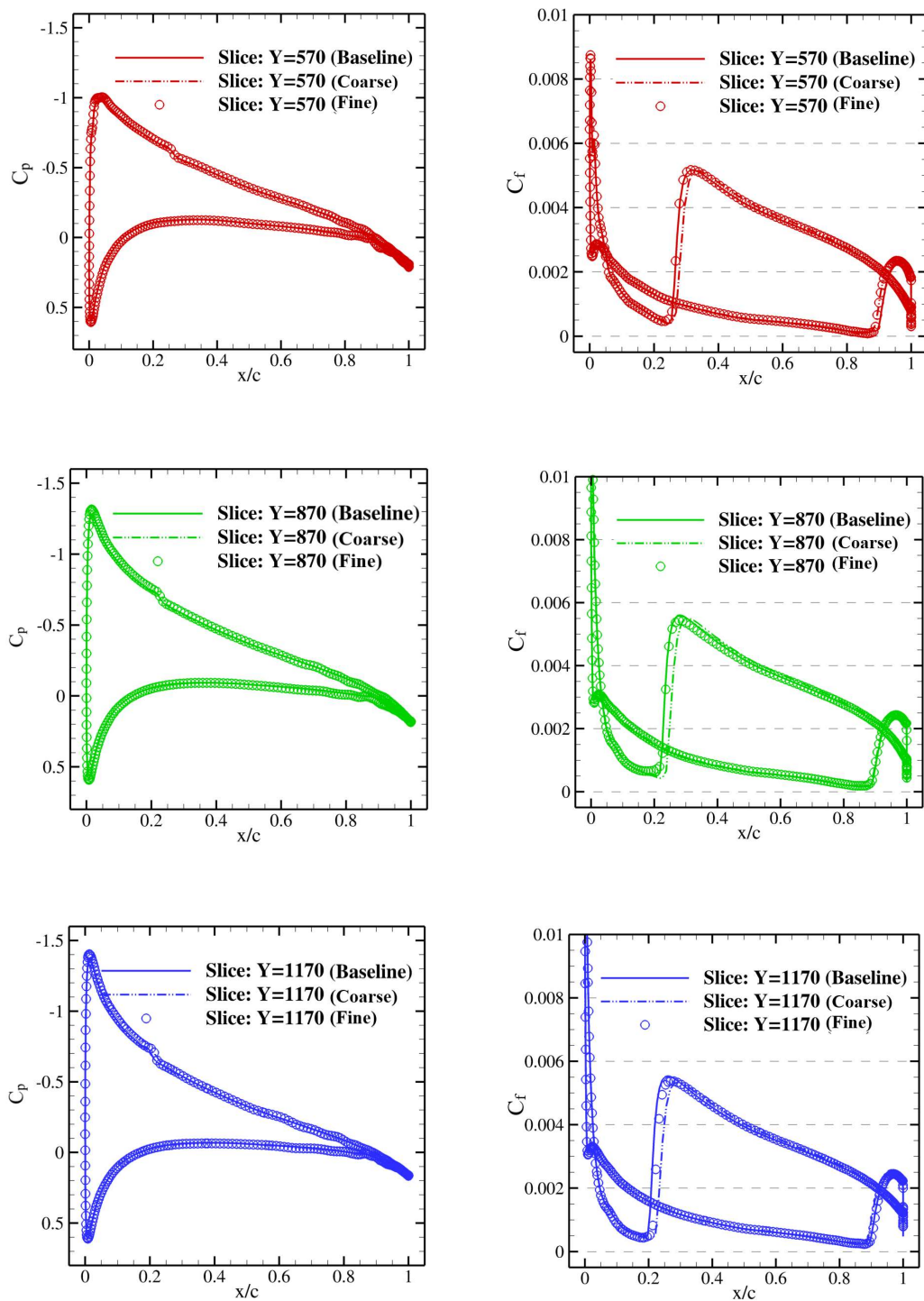
Fig. 5. Comparison of surface pressure and skin-friction distributions at various stations on the wing obtained with an imposed transition on different grid levels for $\alpha = 5°$.

To enable a direct comparison between the predicted transition fronts based on the stability analysis and the RANS-based transition models, respectively, one must ensure that the pressure distributions from those solutions match with each other. To that end, the streamwise pressure distributions at a total of four selected spanwise locations are plotted in Fig. 6 for $\alpha = 0°$ and $\alpha = 7.5°$. It is evident that the solutions with an imposed transition front and the RANS-based transition models indicate an excellent match, with the sole exception of the suction peak pressure level being slightly higher than those from the RANS-based transition models for the case of $\alpha = 7.5°$ in the most inboard section ($y = 270$ mm; see Fig. 6(a)).

(a) y = 270 mm

(b) y = 570 mm

(c) y = 870 mm

(d) y = 1170 mm
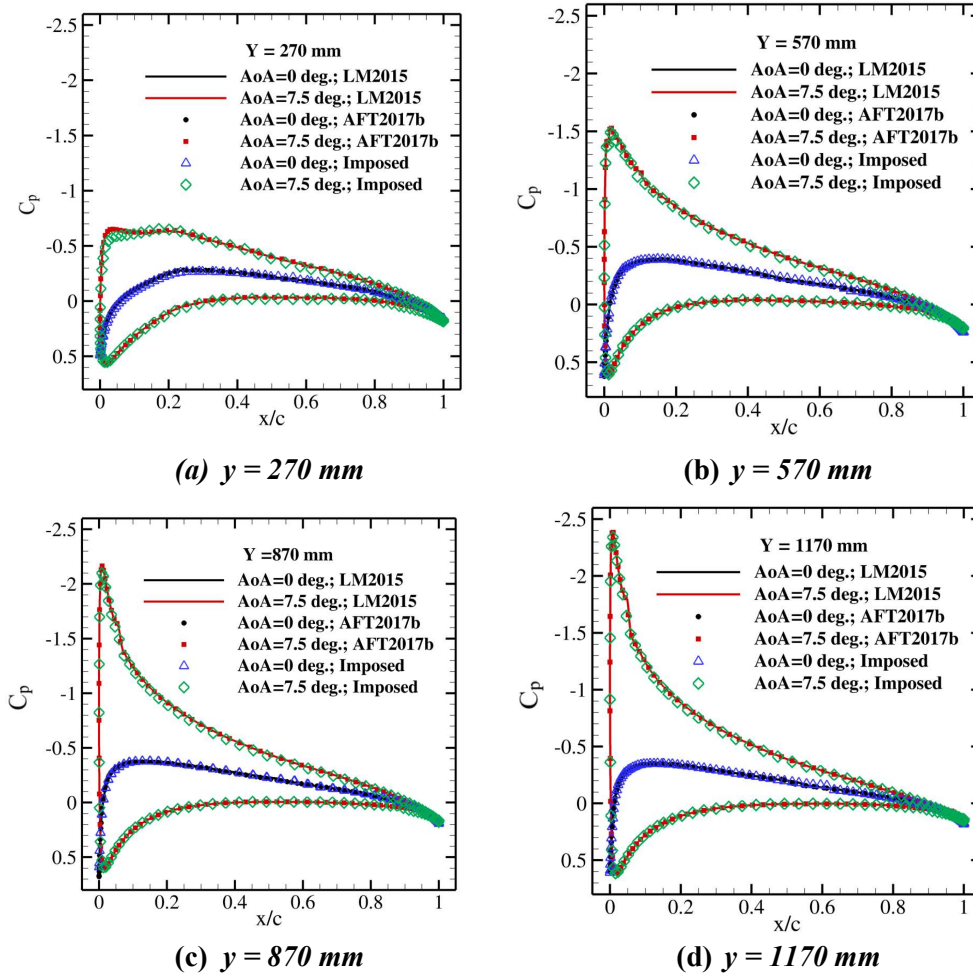
Fig. 6. Comparisons of predicted surface pressure coefficient for $\alpha = 0°$ and $7.5°$ obtained at selected spanwise locations using the SA model with an imposed transition front and RANS-based transition models.

B. Instability Characteristics

The N-factor envelopes obtained with the baseline grid and the nonorthogonal PSE are discussed in this section. Figures. 7–11 display the contours of N_{TS} and N_{CF} within the laminar region of the solutions for $\alpha = 0°, 2.5°, 5°$, and $7.5°$, respectively, for both the upper and the lower surfaces of the wing.

For $\alpha = 0°$, TS amplification appears to dominate the instability on either side of the wing, with N_{TS} values reaching values of greater than 9. The dominance of TS waves is attributed to the moderately adverse streamwise pressure gradient over a majority of the upper and lower surfaces, as seen from the plots in Fig. 4. Crossflow effects appear to be relatively insignificant, as seen from Fig. 7. Ignoring small asymmetries,

11

the N-factor envelopes obtained for both surfaces of the wing at $\alpha = 0°$ are nearly similar. Based on the N_{TS} levels, one expects approximately 50% of the wing to be remain laminar regardless of the spanwise position.

Figure 8 shows that the TS waves continue to be the dominant instability mechanism at $\alpha = 2.5°$. N_{CF} levels do reach a value of around 6 within a small region beyond the midchord location as one approaches the Yehudi break region on the lower surface of the wing. Due to the small shift in pressure distribution relative to the $\alpha = 0°$ condition, as seen from Fig. 4, the region of maximum N_{TS} at $\alpha = 2.5°$ has shifted similarly upstream on the upper surface and downstream on the lower surface, in comparison with the peaks of N_{TS} at $\alpha = 0°$.

(a) Upper surface
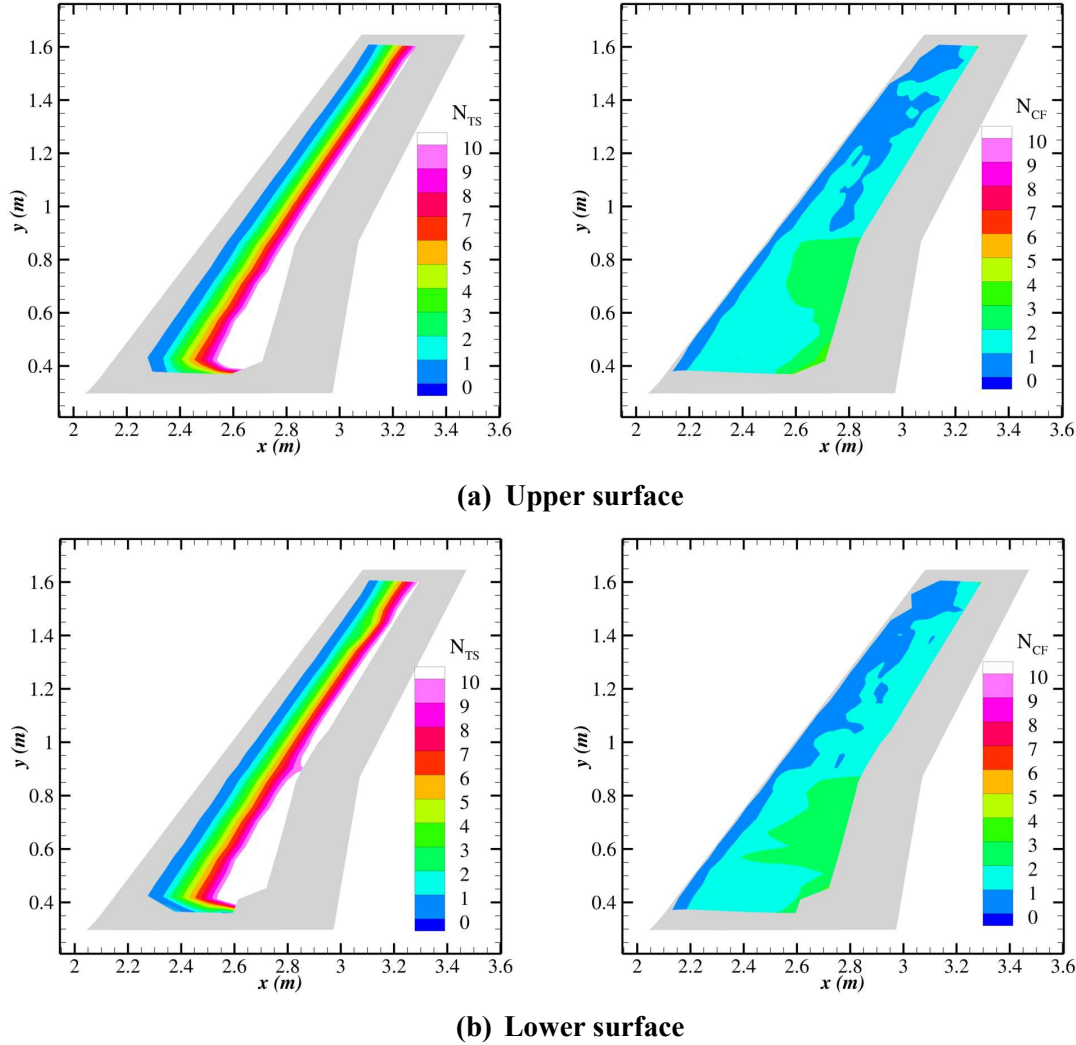
(b) Lower surface

Fig. 7. N-factor contours of TS waves ($\beta = 0$) and stationary CF waves ($f = 0$) calculated with nonorthogonal PSE for $\alpha = 0°$.

As the angle of attack increases to $\alpha = 5°$, the inboard region of the lower surface of the wing starts to indicate a region of large N_{CF} values, signifying significant stationary crossflow effects as observed from Fig. 9. There is a small region on the inboard portion of the wing, 0.4 m $< y <$ 0.8 m and $x >$ 2.6 m, with both large N_{TS} and N_{CF} values (see Fig. 9 (b)), indicating comparable levels of amplification for both types of instability within this region. On the other hand, the TS instability remains dominant on the upper surface of the wing and the location at which $N_{TS} \approx 8$ moves further upstream and closer to the leading edge throughout

the model span, with the contour lines for N_{TS} remaining parallel to the leading edge. The lack of a significant crossflow instability on the upper surface of the wing could be attributed to the rapid acceleration near the leading edge, which is then followed by an adverse pressure gradient. We recall that the α = 5° condition was also chosen for the grid convergence study. Therefore, the N-factor contours obtained from the stability analysis of the mean flow solutions computed using the coarse and fine grids, respectively, are shown in Fig. 10 (where the results for the lower surface alone have been shown for the sake of brevity). The contour plots for the different levels of grid resolution in Figs. 9 and 10 are nearly identical to each other, and therefore, one may conclude that both the mean flow solutions and the results of the stability analysis are indeed insensitive to the level of grid resolution.

(a) Upper surface
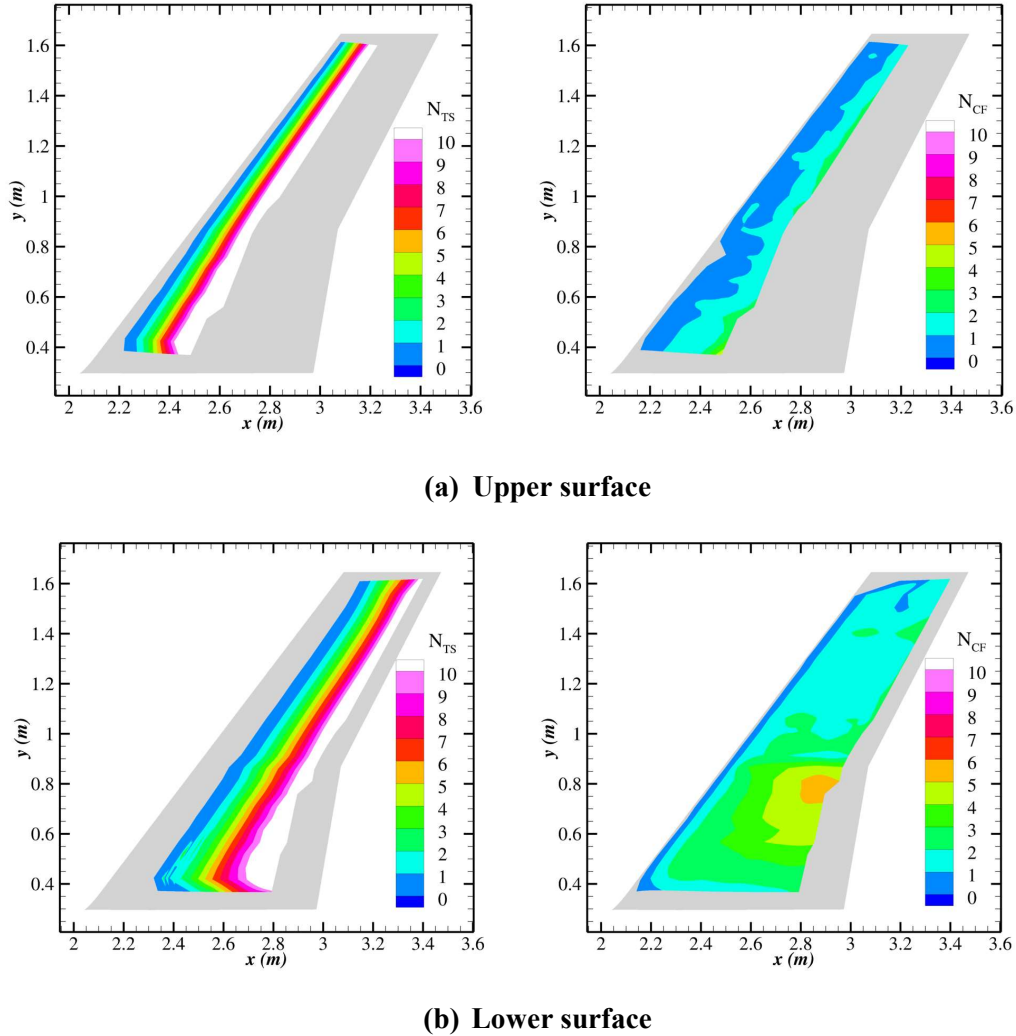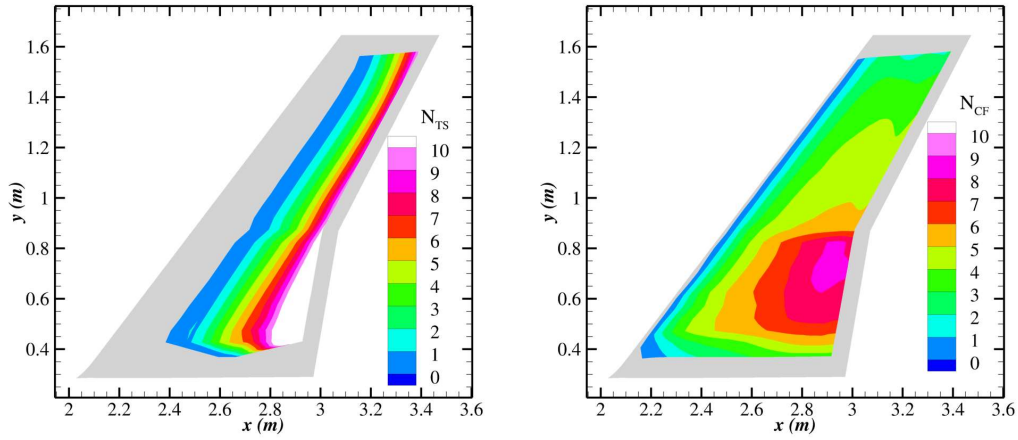
(b) Lower surface

Fig. 8. *N*-factor contours of TS waves ($\beta = 0$) and stationary CF waves ($f = 0$) calculated with nonorthogonal PSE for $\alpha = 2.5°$.
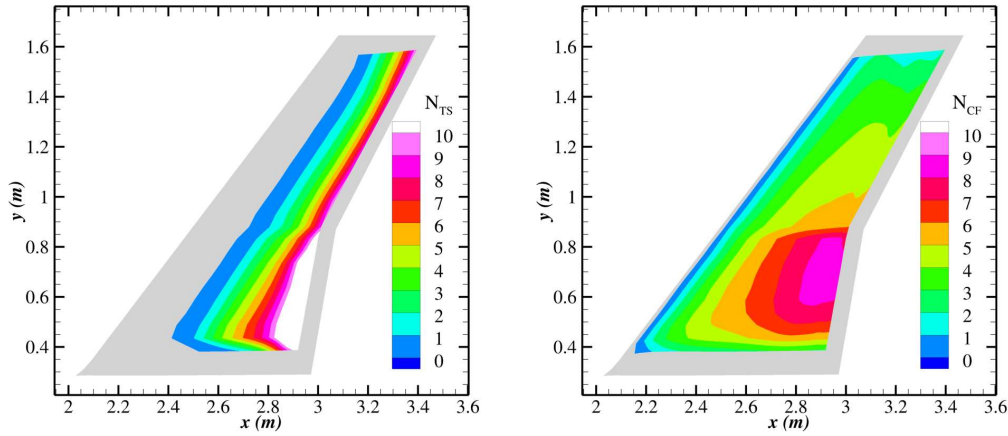
13
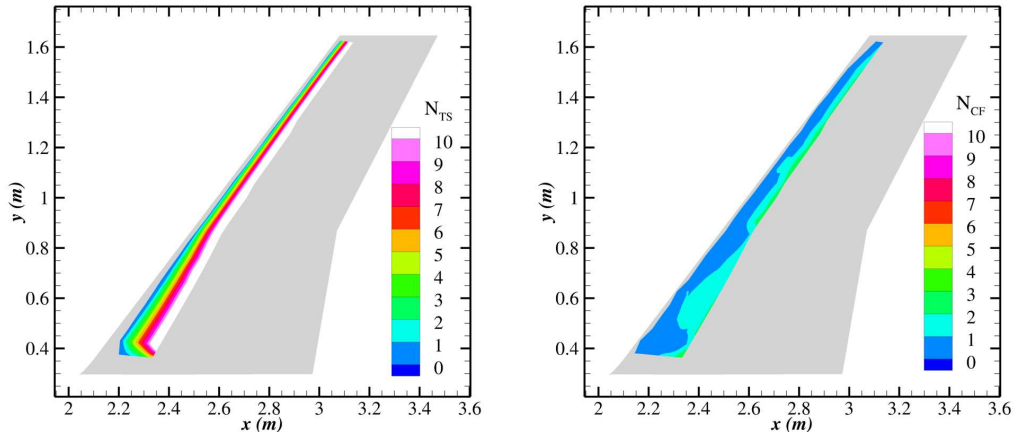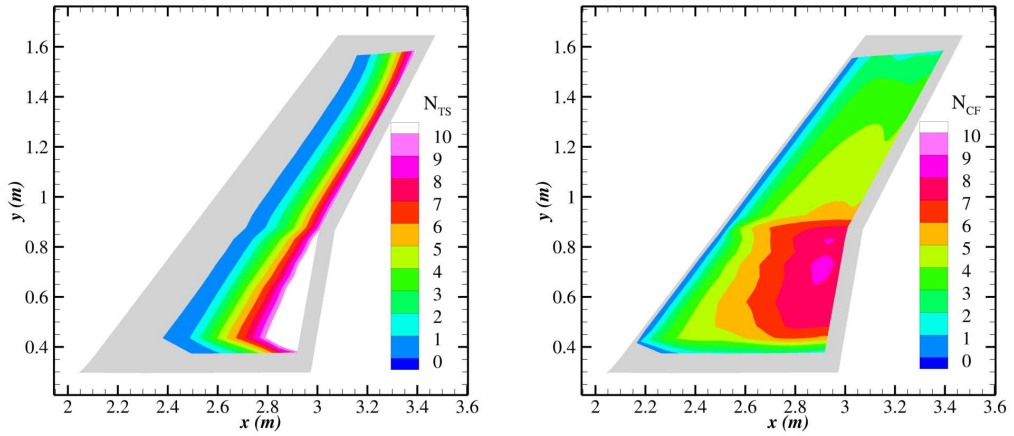
(a) Upper surface

(b) Lower surface

Fig. 9. *N*-factor contours of TS waves $(\beta = 0)$ and stationary CF waves $(f = 0)$ calculated with nonorthogonal PSE for $\alpha = 5°$.

The results for $\alpha = 7.5°$ in Fig. 11 are limited to the shorter laminar region on the upper surface of the wing. Although it may not be easy to discern from this plot, N_{TS} quickly reaches values greater than 7 on the upper surface of the wing for spanwise locations inboard of the region near the crank. Beyond that, due to the limited laminar region, the N_{TS} does not get to a critical value. As a result, we will need to attempt recomputing these results with a slightly larger laminar region. N_{CF} continues to remain insignificant all along the upper surface due to the rapid acceleration near the leading edge followed by a strong adverse pressure gradient (see Fig. 4). On the other hand, on the lower surface of the wing, crossflow effects completely dominate the entire span of the wing as indicated by large regions with N_{CF} values larger than 7. N_{TS} is around 5 for most of the part, with tiny regions experiencing values around 7, thereby indicating that TS is not the main instability mechanism on the lower surface. This could also be attributed to the nearly constant streamwise pressure distribution one saw at various spanwise stations in Fig. 4 on the lower surface for this flow condition. Favorable or zero pressure gradients in general tend to suppress growth of TS-instabilities.
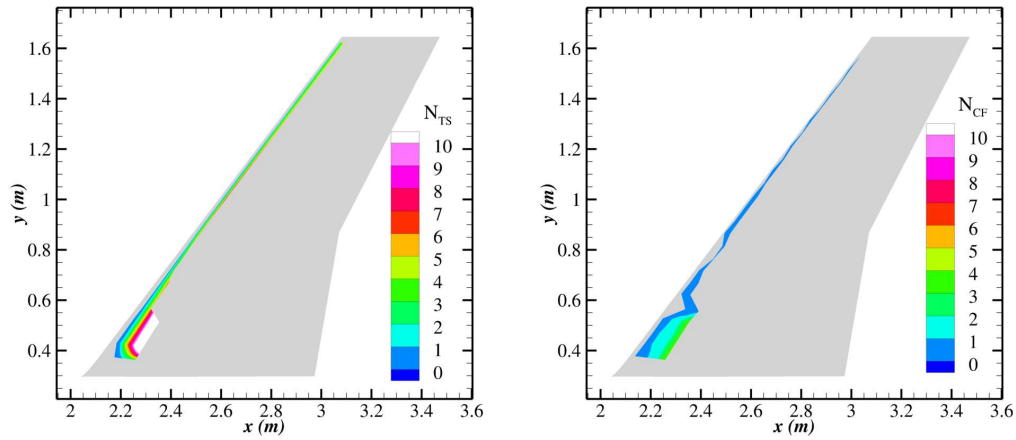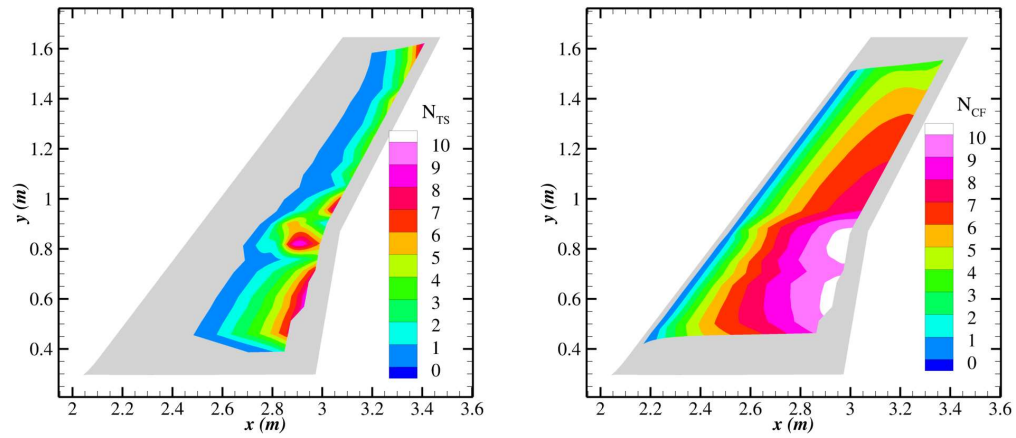
14

(a) Coarse Grid

(b) Fine Grid

Fig. 10. *N*-factor contours of TS waves $(\beta = 0)$ and stationary CF waves $(f = 0)$ calculated with nonorthogonal PSE for the lower surface of the wing at $\alpha = 5°$ using the coarse and fine grids.

Finally, the dual N_{TS}--N_{CF} criterion of Eq. 5 is evaluated by using the PSE results presented above. The critical N_{TS} and N_{CF} are set to 8, based on the disturbance level in the wind tunnel and the assumed roughness level of the model, along with $a_{TS} = 3$ and $a_{CF} = 3$. The predicted transition locations obtained by using these values in Eq. 5 are shown for the different angle of attack flow conditions in Fig. 12 for both the suction and lower surfaces of the wing. One can clearly see that the transition front on the upper surface moves upstream toward the leading edge of the wing with an increase in angle of attack and the front largely remains parallel to the leading edge. For α = 7.5°, due to the limited laminar region, the front on the upper surface appears to terminate prematurely around the crank region. On the other hand, on the lower surface, the transition front does move downstream on the outboard portion of the wing; while on the inboard, the increased crossflow instability seen at higher angles of attack appears to shrink the laminar extent. Thus, the trends shown here nicely encapsulate the various aspects of the instabilities discussed in the preceding paragraphs.
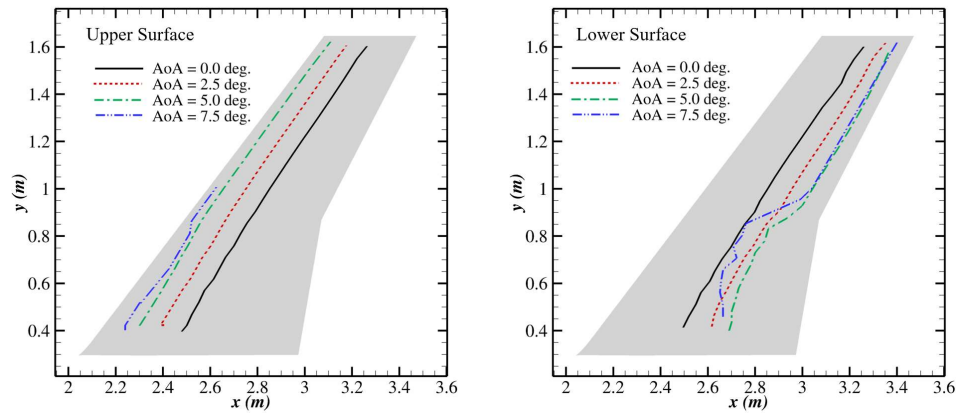
(a) Upper surface

(b) Lower surface

Fig. 11. *N*-factor contours of TS waves ($\beta = 0$) and stationary CF waves ($f = 0$) calculated with nonorthogonal PSE for $\alpha = 7.5°$.

Fig. 12. Predicted transition front using the dual N_{TS} -- N_{CF} criterion for the different flow conditions with $N_{TS,C}$ = 8 and $N_{CF,C}$ = 8.
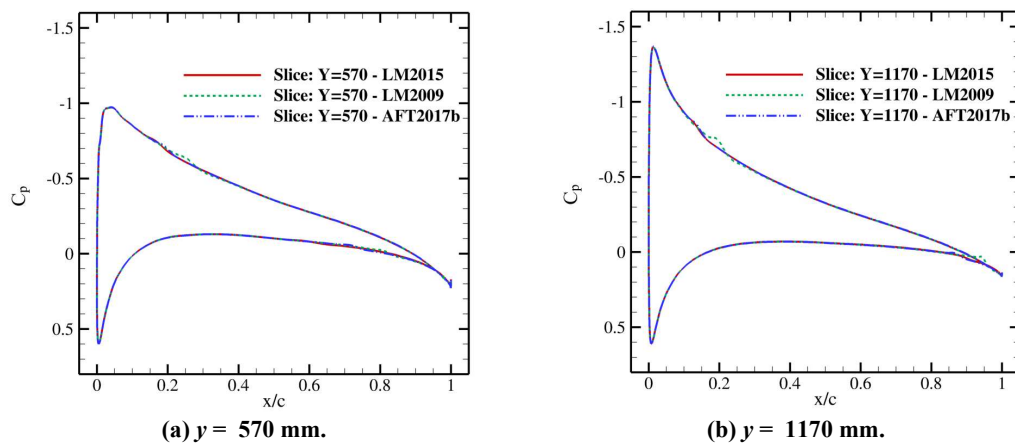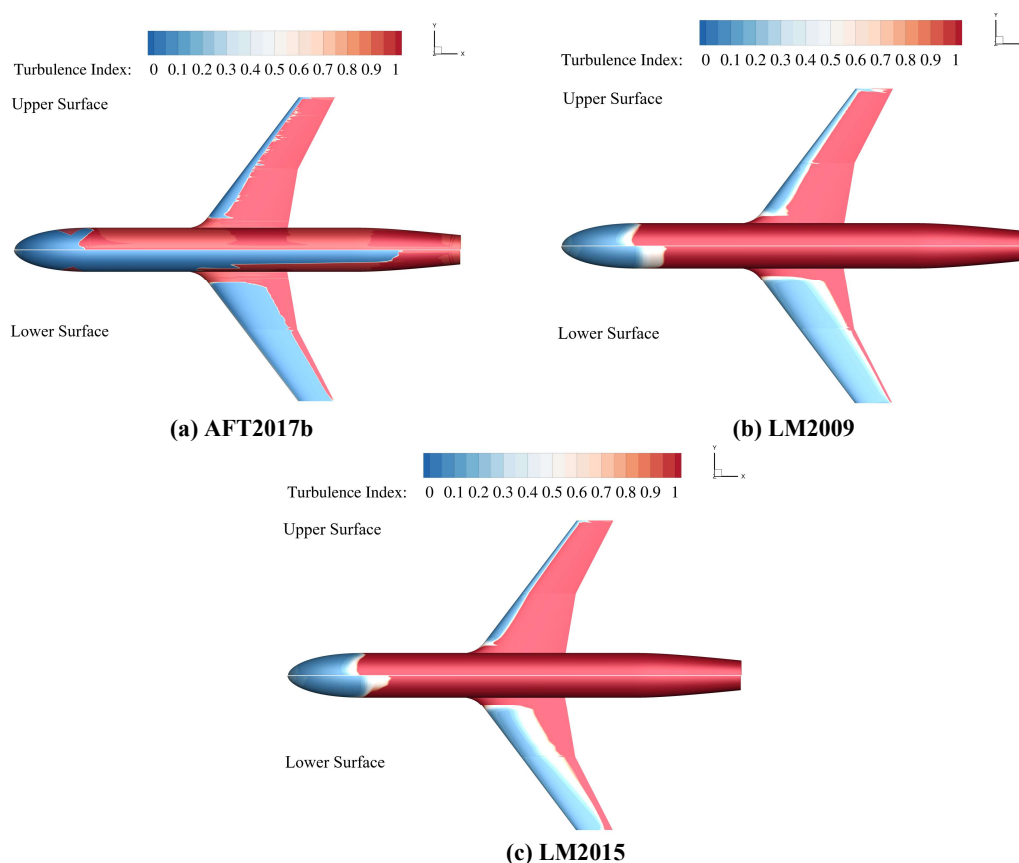
C. RANS-based Transition Model Solutions

In this section, we discuss the results obtained using RANS-based transition models. For the SST-based Langtry-Menter model, FSTI was enforced by using the option to sustain the desired FSTI level in the near field by adding source terms to the SST- model, as put forth by Spalart and Rumsey [52]. This was done by specifying FSTI = 0.08% at the inlet along with $(\mu_t/\mu)_{inlet} = 1$. For the AFT model, the critical amplification factor, N_{crit}, was determined within the model based on the enforced FST = 0.08% using Mack's relationship [54]. Most of the computations, unless specified otherwise, were carried out with the baseline grid.

1. Influence of Transition Model

A preliminary assessment of the suitability of the transition models to this particular problem was carried out by performing computations on the coarse grid for $\alpha = 5°$ using the LM2015 model that accounted for both TS and stationary CF, and the two models that accounted for TS effects alone, namely LM2009 and AFT2017b. The sectional pressure distribution at selected spanwise locations obtained using the different models is shown in Fig. 13 and indicates a good match between the various models, with the exception of a tiny region around where the models predict transition. To understand how this pressure distribution translates in terms of predicted laminar extent, the predicted fronts from the different models are shown in Fig. 14, using turbulence index contours. The turbulence index is an indicator for transition in the CFD computations, the definition for which was originally proposed by Spalart [40]. The definition of the index differs between the SA [40] and SST [55] models , and as a result, in SA-based transition models that value always lies between 0 and 1, while for SST-based transition models, its value does appear to exceed 1 in turbulent regions (values around 2.5 were seen for the computations shown herein) based on our limited experience with it. A turbulence index value of 0.95 (value of 0 indicating laminar regions) and above appears to reasonably indicate the location of transition for this configuration (as it coincides with the location around which the skin friction distribution jumps from its laminar value to the turbulent level). On the upper surface, all three models predict similar transition fronts, given that the flow is dominated by TS-instabilities here. On the lower surface, LM2015 alone predicts a slightly smaller laminar extent in the inboard portion of the wing as one approaches the root of the wing, while very little difference exists between LM2009 and AFT2017b results. This is a consequence of CF-instabilities being dominant in those regions, as was pointed out in the stability analysis and only the LM2015 model accounts for the stationary CF effects. Consequently, for the rest of the study, we will be utilizing the LM2015 model in addition to the AFT2017b model that will serve as a representative model that accounts for TS effects alone (instead of LM2009 model). Picking these two models also allows for use of two different baseline turbulence models.


(a) $y = 570$ mm.　　　　　(b) $y = 1170$ mm.

Fig. 13. Comparison of surface pressure distributions at selected spanwise stations on the wing obtained using different transition models on the coarse grid for $\alpha = 5°$

(a) AFT2017b

(b) LM2009

(c) LM2015

**Fig. 14. Predicted transition behavior as depicted via turbulence index contours for $\alpha = 5°$ obtained using different transition models on the coarse grid.**

2. *Grid Convergence*

To ensure that the solutions computed with these RANS-based transition models are grid converged, the computations were repeated using the coarse, baseline and fine grids for $\alpha = 5°$ using the LM2015 and AFT2017b model. Results from the LM2015 model alone will be shown here for brevity. The streamwise distribution of the pressure coefficient at selected spanwise stations are shown in Fig. 15 and they all collapse well with each other. The more important transition fronts are shown in Fig. 16. On the upper surface of the wing, the transition fronts appear to be grid converged. On the lower surface, there appears to be differences in the inboard region from the side of the body to around the crank, while they appear to be grid converged on the outboard portion of the wing. Investigating further, it was seen that the fronts as predicted by the coarse and baseline grids had converged without changing when the computations were continued, while the front from the fine grid was still changing by small amounts in the region around the crank, indicating that computation was insufficiently converged. Therefore, the results from the fine grid should be considered as preliminary. Also, the results from the baseline grid indicates a sinusoidal front in this region and it was unclear as to what was causing this. Similar slower convergence on the fine grid was also seen with the AFT model. In general, the overall transition fronts in Fig. 16 are very similar to the front predicted based on the stability analysis, thereby giving confidence that the baseline grid should be adequate. For additional confirmation to ensure that the grids were adequate, the coarse and baseline grids were used with both AFT2017b and LM2015 models at the other flow conditions and the resulting fronts from the two different grids did match closely with each other on the upper and lower surfaces of the wing for all the conditions.

18
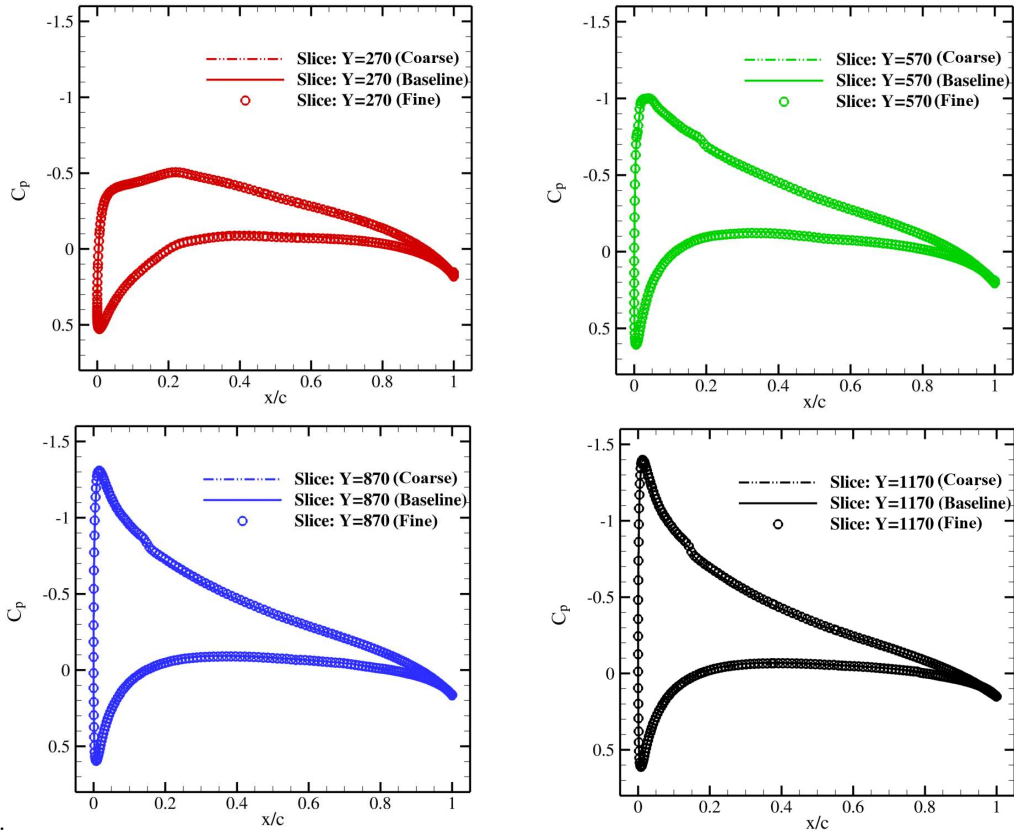
Fig. 15. Comparison of surface pressure distributions at various stations on the wing obtained with LM2015 on different grid levels for $\alpha = 5°$.
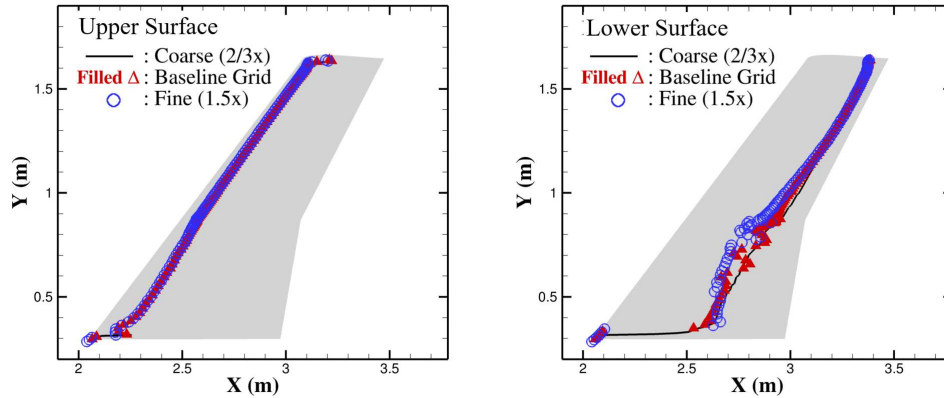

Fig. 16. Transition fronts on the upper and lower surfaces of the NACA 0015 wing as predicted by the LM2015 model with different grids for $\alpha = 5°$.

### 3. Computations at $\alpha = 0°, 2.5°, 5°, and\ 7.5°$

Results from the computations performed with the LM2015 and AFT2017b models for all the flow conditions considered are discussed in this section. Figures 17 – 20 show the turbulence index contours on the model at different flow conditions using the two transition models. Figure 21 provides an overview of the fronts' change with model and angle of attack. As Fig. 17 indicates, at $\alpha = 0°$, there is very little difference in the fronts predicted by the two models, as this flow condition is dominated by TS-instabilities. The AFT2017b model does indicate a region of small oscillation in the transition front around the crank. As the angle of attack increases, one can observe that the fronts predicted by the two models are similar to each other on the

19

upper surface of the wing, with the extent of laminar flow region shrinking with an increase in angle of attack. As was confirmed by the stability analysis, the upper surface of the wing always appears to be dominated by TS-instabilities and hence the reasonable match between LM2015 and AFT2017b results is expected. However, on the lower surface of the wing, one can notice the differences between the fronts predicted by the two models. The AFT2017b consistently predicts an increasing laminar flow extent with an increase in angle of attack (see Fig. 21 (a)), with almost the entire wing being under laminar flow at higher angles of attack. On the other hand, with the LM2015 model (see Fig. 21 (b)), the laminar extent increases only on the outboard portion of the wing. Even within the outboard region, as one moves to $\alpha = 5°$ and $\alpha = 7.5°$, the separation between the fronts shrinks. Furthermore, the inboard section starts to see a reduced laminar flow region with an increase in angle of attack. It was pointed out in the stability analysis section, at $\alpha = 5°$ and $\alpha = 7.5°$, the pressure distribution on the upper surface of the wing is such that it promotes stationary crossflow instabilities and there are also regions of mixed TS-CF instabilities. The results from LM2015 are consistent with those observations. Also, at all angles above 0°, the AFT2017b model always predicts a much larger laminar flow region on the bottom part of the fuselage as compared to the LM2015 model. The forces and the pitching moment coefficients for the computations with the two different transition models for the different flow conditions are listed in Tables 3 and 4. These values compare reasonably well with those from the computations with an imposed transition front. It can also be seen that, as the AFT2017b predicts a larger laminar flow region on the bottom fuselage and the lower surface of the wing, the computed drag coefficient is smaller than that from LM2015.

| (a) AFT2017b | (b) LM2015 |
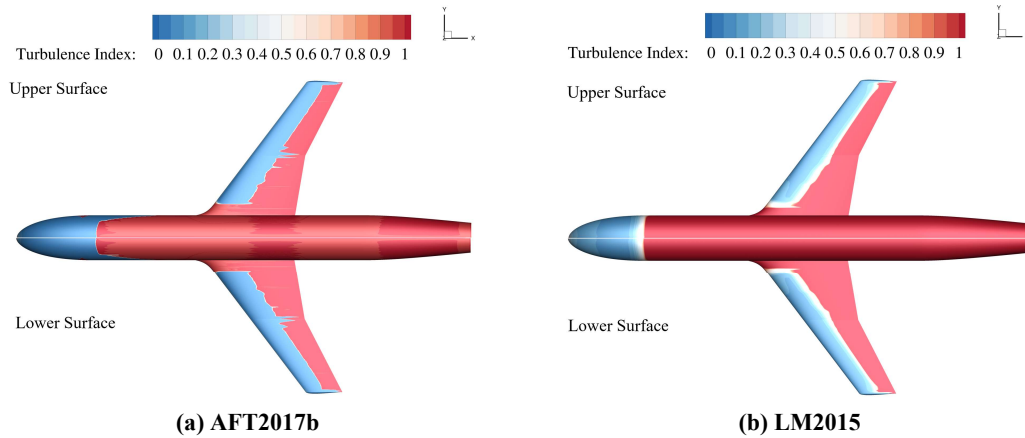
Fig. 17. Predicted transition behavior as depicted via turbulence index contours for $\alpha = 0°$ obtained using different transition models on the baseline grid.

| (a) AFT2017b | (b) LM2015 |
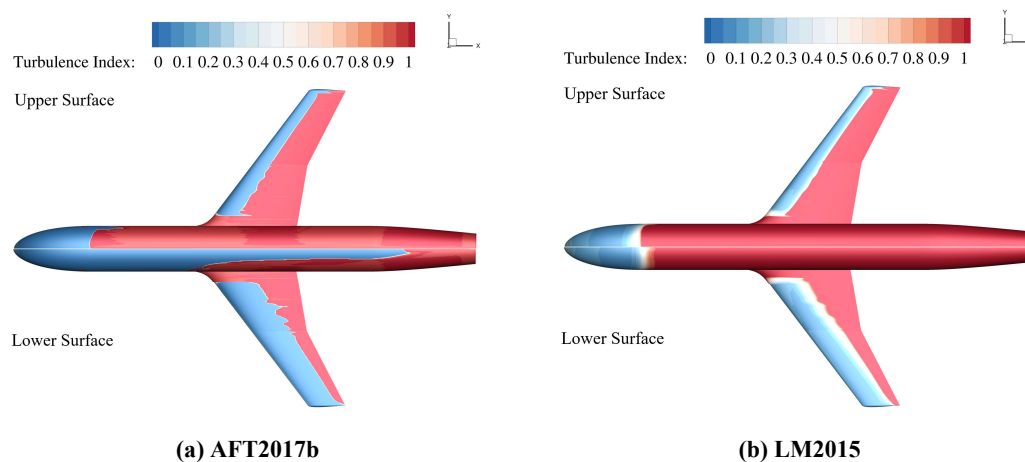
Fig. 18. Predicted transition behavior as depicted via turbulence index contours for $\alpha = 2.5°$ obtained using different transition models on the baseline grid.
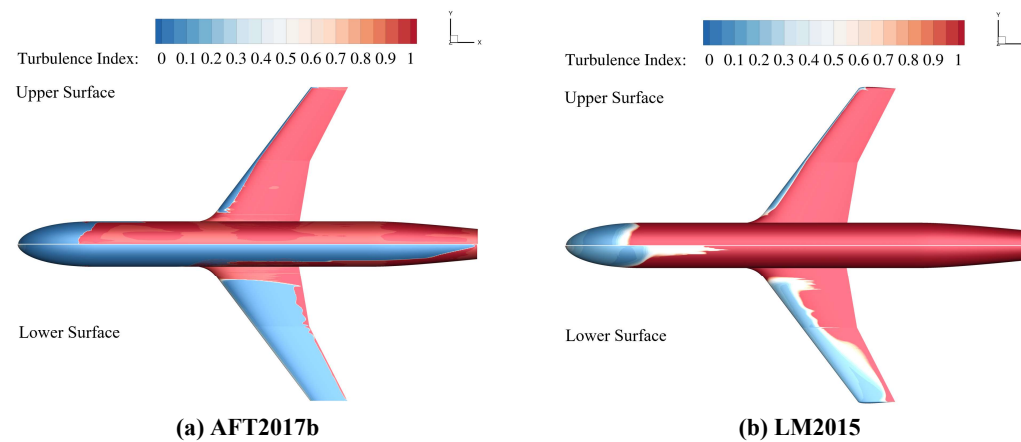
(a) AFT2017b

(b) LM2015
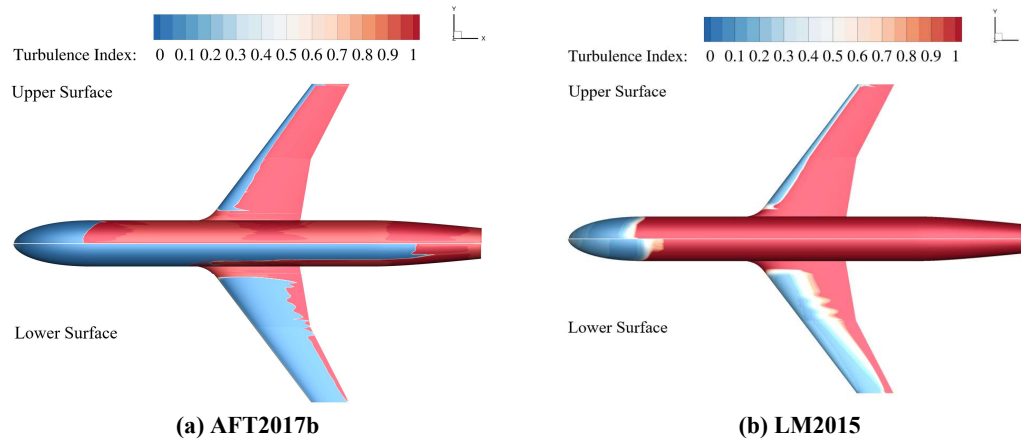
Fig. 19. Predicted transition behavior as depicted via turbulence index contours for $\alpha = 5°$ obtained using different transition models on the baseline grid.


(a) AFT2017b

(b) LM2015

Fig. 20. Predicted transition behavior as depicted via turbulence index contours for $\alpha = 7.5°$ obtained using different transition models on the baseline grid.

Table 3 Force and moment coefficients from the computations using LM2015.

Angle of Attack	C_L	C_D	C_m
$\alpha = 0.0°$	0.00000	0.01977	0.00003
$\alpha = 2.5°$	0.19370	0.02286	-0.01501
$\alpha = 5.0°$	0.39121	0.03081	-0.03473
$\alpha = 7.5°$	0.59305	0.044734	-0.06297

Table 4 Force and moment coefficients from the computations using AFT2017b.

| Angle of Attack	C_L	C_D	C_m
$\alpha = 0.0°$	-0.00023	0.02038	0.00026
$\alpha = 2.5°$	0.19474	0.02271	-0.01511
$\alpha = 5.0°$	0.39227	0.03008	-0.03536
$\alpha = 7.5°$	0.59365	0.04326	-0.06414

(a) AFT2017b

(b) LM2015
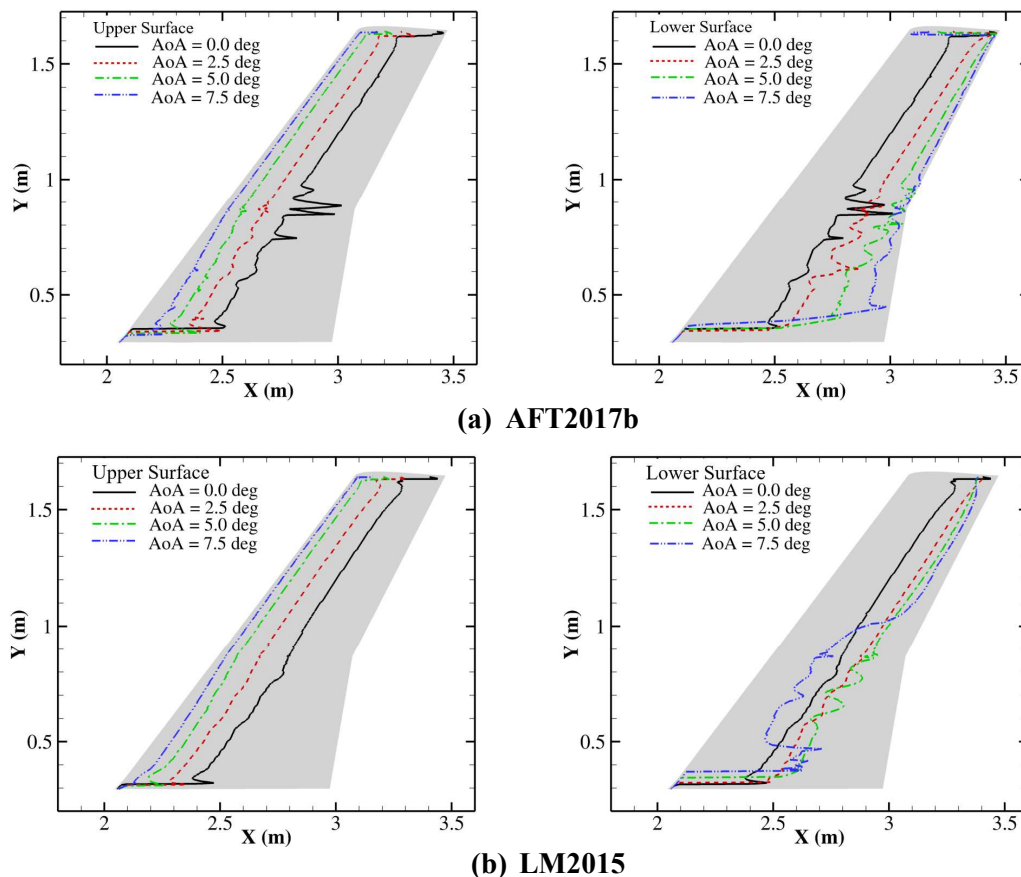
Fig. 21. Variation of predicted transition front with change in angle of attack obtained using different transition models.

To provide an overall comparison between the various results discussed so far, the transition fronts as obtained from the stability analysis are compared against those from the LM2015 model in Fig. 22 for all the flow conditions investigated. On the upper surface of the wing, with TS being the dominant instability mode, the fronts predicted by the transition model appears to closely match that from the stability analysis. The one exception is the result from the stability analysis for $\alpha = 7.5°$, for which the transition front terminated mid-span, because of the small laminar flow region used for mean flow computations in the outboard portion of the wing. These appear to be qualitatively similar to what was observed from the IR imagery shown in Fig. 23, that were obtained in 2016 as part of risk-reduction experiments [3]. Due to lack of precise geometric data about the risk-reduction model and small distortions in the IR images (probably due to the camera angle), the transition front obtained from the computations could not be overlaid on top of these images to provide a more direct measure. However, these images clearly also show that the laminar flow extent on the upper surface of the wing shrinks with an increase in the angle of attack. On the lower surface of the wing, the predicted fronts from LM2015 closely match those from stability analysis in the outboard portion of the wing. In the inboard portion, the transition fronts predicted by the linear stability correlation and the LM2015 model agree well with each other for $\alpha = 0°$ and $\alpha = 2.5°$. However, for $\alpha > 2.5°$, the LM2015 model predicts a slightly smaller laminar flow extent within the inboard region than the corresponding prediction based on the linear stability analysis. No IR images from the risk-reduction experiment were available for the lower surface of the wing. However, because of potentially mixed-mode transition on the lower surface, transition measurements on that surface are expected to provide valuable data toward the calibration (or assessment) of the various transition models.
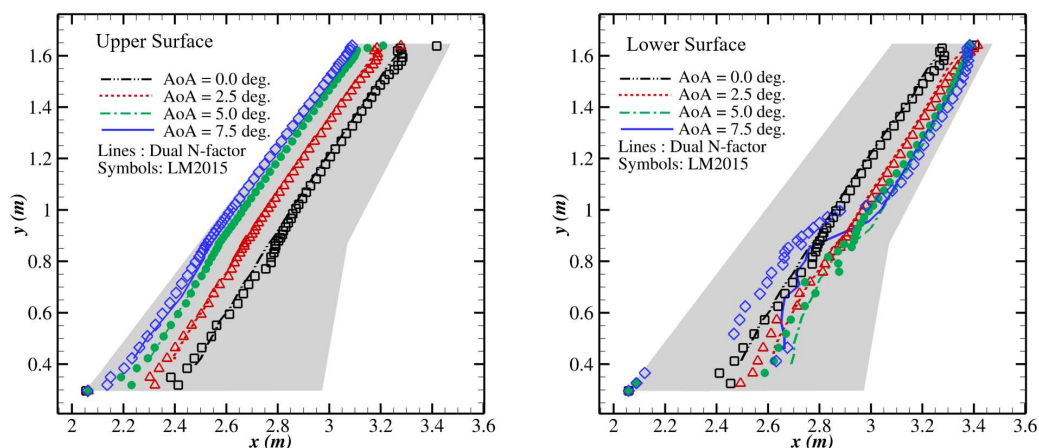
Fig. 22. Transition fronts on the upper and lower surfaces of the NACA 0015 wing as predicted by stability analysis and LM2015 model. Lines indicate results from the stability analysis using the dual $N_{TS} - NT_{CF}$ criterion and the symbols correspond to LM2015 results. Lines and symbols corresponding to an angle of attack are in the same color.
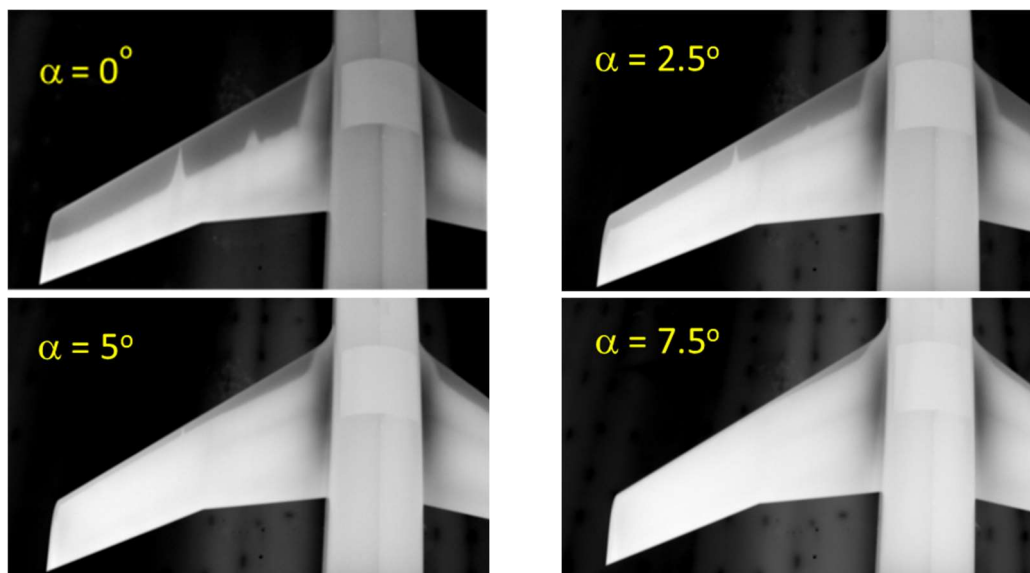
Fig. 23. IR Imagery of the upper surface of the NACA 0015 wing from the risk-reduction Experiment [3] at different flow conditions.

Given the focus of the NASA Juncture Flow experiment on the flow separation near the wing-juncture region near the trailing edge, the contours of skin-friction at the model surface are shown in Fig. 24, for the case of the LM2015 transition model and an angle of attack equal to 7.5 degrees. In this plot, a cut-off below 0 has been applied to the contour levels to identify the separated flow region; the wing-juncture region near the trailing edge that appears in gray/white color represents the separated flow region. As indicated in Fig. 24, one does see a small, separated flow region near the wing juncture trailing edge region even in the case of an NACA 0015-based wing. For all of the flow conditions investigated in this work, there was a small, separated region near the wing juncture close to the trailing edge on the upper surface of the wing (and also on the lower surface for $\alpha = 0°$). The region of separation had the smallest extent for $\alpha = 0°$, with the length of the region in the streamwise direction being around 54 mm and 5 mm in the spanwise direction. For the remaining conditions, the separation region was approximately 67 mm long in the streamwise direction (larger by 24% as compared to $\alpha = 0°$) and 8mm wide in the spanwise direction (larger by 60% as compared to $\alpha = 0°$). It remains to be investigated how these bubble sizes compare to computations performed under

23

the assumption of being fully turbulent everywhere, to evaluate the impact of transition. Another aspect that deserves mention is that, in all the computations performed, one did not encounter any laminar separation, as the boundary layer naturally transitioned upstream of where a nominally laminar boundary layer would have separated.
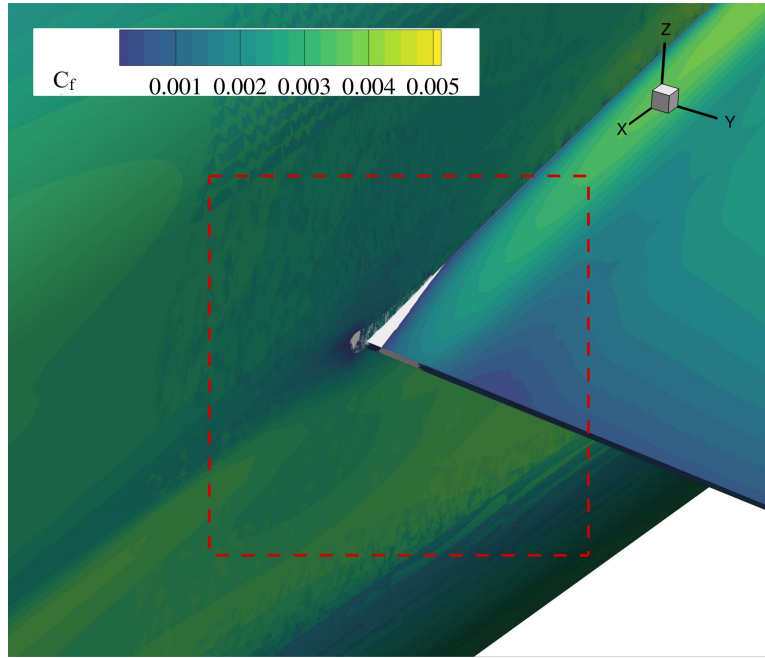
Fig. 24. Contours of skin friction (cut-off applied for values below 0) on the model surface to indicate regions of separated flow for an angle of attack equal to +7.5 degrees. The trailing-edge region around the wing-juncture has been highlighted for convenience.

VI. Concluding Remarks

Pretest computational assessment of boundary layer transition on the NASA Juncture flow model with the NACA 0015-based wing was carried out for a selected set of flow conditions. The transition analysis was performed via two different approaches involving NASA's OVERFLOW 2.3b CFD solver and the LASTRAC stability solver, namely, (i) LASTRAC based PSE marching along the streamline based on a partially laminar basic state obtained from OVERFLOW 2.3b by using the SA turbulence model along with an imposed transition front; and (ii) the RANS-based SA-AFT2017b and SST-2003-LM2009/LM2015 models within OVERFLOW 2.3b.

The stability computations revealed that the upper surface of the wing is dominated by TS-instabilities at all angles of attack within the range of $0° \leq \alpha \leq 7.5°$, with the laminar flow extent being as large as 50% chord at $\alpha = 0°$ but steadily shrinking with an increasing angle of attack. At $\alpha = 7.5°$, the laminar flow region is predicted to be rather small, with transition happening within a short distance downstream of the attachment line. On the lower surface of the wing, TS-instability continues to be the dominant mode across the entire wing span for $\alpha = 0°$ and $\alpha = 2.5°$. At higher angles of attack, the CF instability starts to dominate within the inboard portion of the wing and in regions around the crank. The inboard region also displays mixed TS-CF instability. The extent of laminar flow region on the outboard region of the lower surface is predicted to increase with the angle of attack for all angles considered herein and consistently covers more than 50% of the wing chord. At higher angles of attack alone, the laminar flow region in the inboard portion of the lower surface of the wing starts to reduce with an increase in angle of attack due to the growing influence of CF instability in this region, arising from the slightly favorable pressure distribution.

Given the dominance of the TS instability on the upper surface of the wing, both the AFT2017b model and the LM2015 model yielded very similar predictions for the transition front, and those predictions also

compared well with the transition front predicted by the stability analysis based on the dual $N_{TS} - N_{CF}$ criterion at all the flow conditions considered herein. They also compared qualitatively well with the IR images obtained during the risk-reduction experiments. However, as the AFT2017b model does not account for stationary CF effects, it was unable to predict the reduction in the laminar flow extent within the inboard spanwise region on the lower surface of the wing when the crossflow effects became significant at $\alpha = 5°$ and 7.5°. On the other hand, the LM2015 model that includes the crossflow extension was able to correctly predict the upstream shift in transition location within that part of the wing. However, in comparison with the transition front based on the stability analysis, the LM2015 model indicated a slightly earlier transition within the inboard portion of the wing at $\alpha = 5°$ and 7.5°. In that regard, it would be interesting to evaluate the predictions of other crossflow transition models that account for the CF effects without relying on input information regarding the surface roughness, unlike the LM2015 model. Exploring the sensitivity of the model to assumed roughness levels will also be useful to determine the appropriate "equivalent" roughness parameter that will provide good matches in predicted transition front against those based on stability analysis and from the experiment. Another aspect that remains to be investigated is the influence of attachment-line instabilities. Additionally, studying the influence of Reynolds number is also likely to help characterize conditions under which laminar separation is most likely to occur. Overall, the reasonable comparison between the transition front predicted by the stability analysis and the LM2015 model provides increased confidence that the data produced from this study will better inform the planned wind tunnel test. When the actual wind tunnel test is completed and data becomes available, we will perform a more detailed quantitative assessment of the transition fronts predicted by these transition models against measured data and help improve the transition models.

Acknowledgments

References

[1] Slotnick, J., Khodahoust, A., Alonso, J., Darmofal, D., Gropp, W., and Mavriplis, D., "CFD Vision 2030 Study: A Path to Revolutionary Computational Aerosciences," NASA/CR-2014-218178, 2014.

[2] Rumsey, C., Neuhart, D., and Kegerise, M., "The NASA Juncture Flow Experiment: Goals, Progress, and Preliminary Testing," AIAA Paper 2016–1557, 2016.

[3] Kegerise, M. A. and Neuhart, D. H., "Wind Tunnel Test of a Risk-Reduction Wing/Fuselage Model to Examine Juncture-Flow Phenomena," NASA TM–219348, November 2016, https://ntrs.nasa.gov/archive/nasa/casi.ntrs.nasa.gov/20160014854.pdf.

[4] Rumsey, C. L., Carlson, J. R., Hannon, J. A., Jenkins, L. N., Bartram, S. M., Pulliam, T. H., and Lee, H. C., "Boundary Condition Study for the Juncture Flow Experiment in the NASA Langley 14x22-Foot Subsonic Wind Tunnel," AIAA Paper 2017-4126, 2017.

[5] Rumsey, C. L., "The NASA Juncture Flow Test as a Model for Effective CFD/Experimental Collaboration," AIAA Paper 2018-3319, 2018..

[6] Kegerise, M. A. and Neuhart, D. H., "An Experimental Investigation of a Wing-Fuselage Junction Model in the NASA Langley 14- by 22-Foot Subsonic Tunnel," NASA TM–2019-220286, June 2019, https://ntrs.nasa.gov/archive/nasa/casi.ntrs.nasa.gov/ 20190027403.pdf.

[7] Lynde, M. N., and Campbell, R. L., "Computational Design and Analysis of a Transonic Natural Laminar Flow Wing for a Wind Tunnel Model," AIAA Paper 2017-3058, 2017.

[8] Rivers, M., Lynde, M., Campbell, R., Viken, S., Chan, D., Watkins, A., and Goodliff, S., "Experimental Investigation of the NASA Common Research Model with a Natural Laminar Flow Wing in the NASA Langley National Transonic Facility", AIAA Paper 2019-2189, 2019.

[9] Lynde, M. N., Campbell, R. L., Rivers, M. B., Viken, S. A., Chan, D. T., Watkins, A. N., and Goodliff, S. L., "Preliminary Results from an Experimental Assessment of a Natural Laminar Flow Design Method," AIAA Paper 2019-2298, 2019.

[10] Lynde, M. N., Campbell, R. L., and Viken, S. A., "Additional Findings from the Common Research Model Natural Laminar Flow Wind Tunnel Test", AIAA Paper 2019-2298, 2019.

[11] Warren, E. S., and Hassan, H. A., "Transition Closure Model for Predicting Transition Onset," *Journal of Aircraft*, Vol. 35, No. 5, 1998, pp. 769-775.

[12] Edwards, J. R., Roy, C. J., Blottner, F. G., and Hassan, H. A., "Development of a One-Equation Transition/Turbulence Model," *AIAA Journal*, Vol. 39, No. 9, 2001, pp. 1691-1698.

[13] Walters, D. K., and Leylek, J. H., "A New Model for Boundary-Layer Transition Using a Single-Point RANS Approach," *ASME J. of Turbomach*, Vol. 126, No.1, 2004, pp. 193–202.

[14] Menter, F. R., Langtry, R. B., and Völker, S., "Transition Modelling for General Purpose CFD Codes," *J. Flow, Turbulence and Combustion,* Vol.77, 2006, pp.277–303.

[15] Langtry, R. B., and Menter, F. R., "Correlation-Based Transition Modeling for Unstructured Parallelized Computational Fluid Dynamics Codes," *AIAA Journal*, Vol. 47, No. 12, 2009, pp.2894–2906.

[16] Medida, S., and Baeder, J., "Application of the Correlation-based the γ-$Re_{\theta t}$ Transition Model to the Spalart-Allmaras Turbulence Model", AIAA Paper 2011-3979, 2011.

[17] Ge, X., Arolla, S., and Durbin, P., "A Bypass Transition Model Based on the Intermittency Function," *J. Flow Turbulence and Combustion,* Vol.93, 2014, pp. 37–61.

[18] Song Fu, A., Wang, L., "RANS modeling of high-speed aerodynamic flow transition with consideration of stability theory", *Progress in Aerospace Sciences*, Vol. 58, 2013, pp. 36-59.

[19] Coder, J.G., and Maughmer, M.D., "Computational Fluid Dynamics Compatible Transition Modeling Using an Amplification Factor Transport Equation," *AIAA Journal*, Vol. 52, No. 11, 2014, pp.2506–2512.

[20] Coder, J.G., "Further Development of the Amplification Factor Transport Transition Model for Aerodynamic Flows," AIAA Paper 2019-0039, 2019.

[21] Krumbein, A., Krimmelbein, N., Grabe, C. and Shengyang, N., "Development and Application of Transition Prediction Techniques in an Unstructured CFD Code," AIAA Paper 2015-2476, 2015.

[22] Smith, A. M. O., and Gamberoni, N., "Transition, Pressure Gradient and Stability Theory," Douglas Aircraft Company, Long Beach, Calif. Rep. ES 26338, 1956.

[23] van Ingen, J. L., "A Suggested Semi-Empirical Method for the Calculation of the Boundary Layer Transition Region," University of Delft, Dept. of Aerospace Engineering, Delft, The Netherlands, Rep. VTH-74, 1956.

[24] Drela, M. and Giles, M. B., "Viscous-Inviscid Analysis of Transonic and Low Reynolds Number Airfoils," *AIAA Journal*, Vol. 25, No. 10, 1987, pp. 1347–1355.

[25] Drela, M., "Implicit Implementation of the Full e^N Transition Criterion," AIAA Paper 2003-4066, 2003.

[26] Herbert, T., "Parabolized Stability Equations," *Annu. Rev. Fluid Mech.,* Vol. 29, 1997, pp.245-283.

[27] Medida, S., "Correlation-based Transition Modeling for External Aerodynamic Flows," University of Maryland PhD Dissertation, 2014.

[28] Krumbein, A., Krimmelbein, N., Grabe, C. and Shengyang, N., "*Development and Application of Transition Prediction Techniques in an Unstructured CFD Code,*" AIAA Paper 2015-2476, 2015.

[29] Nichols, R. H, and Buning, P. G., "User's Manual for OVERFLOW 2.3, Version 2.3," NASA Langley Research Center, Hampton, VA, Oct 2019. https://overflow.larc.nasa.gov/users-manual-for-overflow-2-3/.

[30] Chang, C.-L., "LASTRAC.3d: Transition Prediction in 3D Boundary Layers," AIAA Paper 2004-2542, 2004.

[31] Chang, C.-L., "Langley Stability and Transition Analysis Code (LASTRAC) Version 1.2 User Manual," NASA TM-2004-213233, June 2004. https://ntrs.nasa.gov/api/citations/20040082550/downloads/20040082550.pdf.

[32] Venkatachari, B. S., Paredes, P., Derlaga, J. M., Buning, P., Choudhari, M., Li, F., and Chang, C. L., "Assessment of Transition Modeling Capability in OVERFLOW with Emphasis on Swept-Wing Configurations," AIAA Paper 2020- 1034, 2020.

[33] Venkatachari, B. S., Paredes, P., Derlaga, J. M., Buning, P., Choudhari, M., Li, F., and Chang, C. L., "Assessment and Improvement of RANS-based Transition Models based on Experimental Data of the Common Research Model with Natural Laminar Flow," AIAA Paper 2021-1430, 2021.

[34] Paredes, P., Venkatachari, B., Choudhari, M., Li, F., Hildebrand, N., and Chang, C. L., "Transition Analysis for the CRM-NLF Wind Tunnel Configuration," AIAA Paper 2021-1431, 2021

[35] Horstmann, K., Redeker, G., Quast, A., Dressler, U., and Bieler, H., "Flight Test with a Natural Laminar Flow Glove on a Transport Aircraft," AIAA Paper 90-3044, 1990.

[36] Arnal, D., "Boundary Layer Transition: Prediction Based on Linear Theory," Special course on Progress in Transition Modeling. AGARD. R-793, 1994, pp. 1–62.

[37] Menter, F. R., "Two-Equation Eddy-Viscosity Turbulence Models for Engineering Applications," *AIAA Journal*, Vol. 32, No. 8, 1994, pp. 1598-1605.

[38] Menter, F. R., Kuntz, M., and Langtry, R., "Ten Years of Industrial Experience with the SST Turbulence Model," *Turbulence, Heat and Mass Transfer*, Vol. 4, No. 1, 2003, pp. 625 - 632.

[39] Langtry, R. B., Sengupta, K., Yeh, D. T., and Dorgan, A. J., "Extending the γ-$Re_{\theta t}$ Correlation based Transition Model for Crossflow Effects," AIAA Paper 2015-2474, 2015.

[40] Spalart, P. R. and Allmaras, S. R., "A One-Equation Turbulence Model for Aerodynamic Flows," *Recherche Aerospatiale*, No. 1, 1994, pp. 5-21.

[41] Choi, J. H., and Kwon, O. J., "Recent Improvement of a Correlation-based Transition Model for Simulating Three-Dimensional Boundary Layers", *AIAA Journal*, Vol. 55, No. 6, 2017, pp. 2103–2108.

[42] Medida, S., and Baeder, J., "A New Crossflow Transition Onset Criterion for RANS Turbulence Models," AIAA Paper 2013-3081, 2013.

[43] Nie, S., Krimmelbein, N., Krumbein, A., and Grabe, C., "Extension of a Reynolds-Stress-Based Transition Transport Model for Crossflow Transition," *Journal of Aircraft*, Vol. 55, No. 1, 2018, pp. 1641–1654.

[44] Grabe, C., Shengyang, N., and Krumbein, A., "Transport Modeling for the Prediction of Crossflow Transition," *AIAA Journal*, Vol. 56, No. 8, 2018, pp. 3167–3178.

[45] Choi, J., and Kwon, O. J., "Enhancement of a Correlation-Based Transition Turbulence Model for Simulating Crossflow Instability", AIAA Paper 2014-1133, 2014.

[46] Carnes, J. A., and Coder, J. G., "Effect of Crossflow on the S-76 and PSP Rotors in Hover," AIAA Paper 2020-0773, 2020.

[47] Neuhart, D. H., and McGinley, C. B., "Free-Stream Turbulence Intensity in the Langley 14- by 22-Foot Subsonic Tunnel," NASA TP 213247, August 2004.

[48] Dagenhart, J. R., Saric, W. S., Mousseux, M. C., and Stack, J. P., "Crossflow-Vortex Instability and Transition on a 45-Degree Swept Wing," AIAA Paper 89-1892, 1989.

[49] Roe, P. L., "Approximate Riemann Solvers, Parameter Vectors, and Difference Schemes," *J. Comput Phys.,* Vol. 43, No. 2, 1981, pp. 357–372.

[50] Nichols, R. H., Tramel, R. W., and Buning, P. G., "Solver and Turbulence Model Upgrades to OVERFLOW 2 for Unsteady and High-Speed Applications," AIAA Paper 2006-2824, 2006.

[51] Shur, M. L., Strelets, M. K., Travin, A. K., and Spalart, P. R., "Turbulence Modeling in Rotating and Curved Channels: Assessing the Spalart-Shur Correction," *AIAA Journal*, Vol. 38, No. 5, 2000, pp. 784–792.

[52] Spalart, P. R., "Strategies for Turbulence Modelling and Simulation," *International Journal of Heat and Fluid Flow*, Vol. 21, 2000, pp. 252–263.

[53] Spalart, P. R. and Rumsey, C. L., "Effective Inflow Conditions for Turbulence Models in Aerodynamic Calculations," *AIAA Journal*, Vol. 45, No. 10, 2007, pp. 2544-2553.

[54] Mack, L. M., "Transition and Laminar Instability," *NASA CR-153203*, May 1977.

[55] Sclafani, A., Slotnick, J., Vassberg, J. and Pulliam, T., "Extended OVERFLOW Analysis of the NASA Trap Wing Wind Tunnel Model," AIAA Paper 2012-2919, 2012.